



The Exotic Type Ic Broad-lined Supernova SN 2018gep: Blurring the Line between Supernovae and Fast Optical Transients

T. A. Pritchard¹ , Katarzyna Bensch², Maryam Modjaz¹ , Marc Williamson¹ , Christina C. Thöne² , J. Vinkó^{3,4,5} , Federica B. Bianco^{6,7,8} , K. Azalee Bostroem⁹, Jamison Burke^{10,11} , Rubén García-Benito² , L. Galbany¹² , Daichi Hiramatsu^{10,11} , D. Andrew Howell^{10,11} , Luca Izzo¹³ , D. Alexander Kann² , Curtis McCully^{10,11} , Craig Pellegrino^{10,11} , Antonio de Ugarte Postigo^{2,13}, Stefano Valenti⁹ , Xiaofeng Wang^{14,15} , J. C. Wheeler¹⁶ , Danfeng Xiang¹⁴ , K. Sárneczky³ , A. Bódi^{3,5,17} , B. Cseh³, D. Tarczay-Nehéz^{3,17} , L. Kriskovics^{3,5}, A. Ordasi³, A. Pál^{3,5} , R. Szakáts³ , and K. Vida^{3,5}

¹ Center for Cosmology and Particle Physics, New York University, 726 Broadway, NY, NY 11201, USA; tapritchard@nyu.edu, tylerapritchard@gmail.com

² Instituto de Astrofísica de Andalucía, IAA-CSIC, Glorieta de la Astronomía, S/N, E-18008, Granada, Spain

³ CSFK Konkoly Observatory, Konkoly Thege M. ut 15–17, Budapest, 1121, Hungary

⁴ Department of Optics & Quantum Electronics, University of Szeged, Dóm tér 9, Szeged, 6720, Hungary

⁵ ELTE Eötvös Loránd University, Institute of Physics, Pázmány Péter sétány 1/A, Budapest, 1117, Hungary

⁶ Department of Physics and Astronomy, University of Delaware, Newark, DE 19716, USA

⁷ Joseph R. Biden, Jr. School of Public Policy and Administration, University of Delaware, Newark, DE 19716, USA

⁸ Data Science Institute, University of Delaware, Newark, DE 19716, USA

⁹ Department of Physics, University of California, Davis, CA 95616, USA

¹⁰ Las Cumbres Observatory, 6740 Cortona Drive, Suite 102, Goleta, CA 93117–5575, USA

¹¹ Department of Physics, University of California, Santa Barbara, CA 93106–9530, USA

¹² Departamento de Física Teórica y del Cosmos, Universidad de Granada, E-18071 Granada, Spain

¹³ DARK, Niels Bohr Institute, University of Copenhagen, Lyngbyvej 2, DK-2100 Copenhagen, Denmark

¹⁴ Physics Department, Tsinghua University, Beijing, 100084, People's Republic of China

¹⁵ Beijing Planetarium, Beijing Academy of Science and Technology, Beijing 100044, People's Republic of China

¹⁶ Department of Astronomy, University of Texas at Austin, Austin, TX 78712, USA

Received 2020 July 31; revised 2021 April 16; accepted 2021 April 20; published 2021 July 15

Abstract

In the last decade a number of rapidly evolving transients have been discovered that are not easily explained by traditional supernova models. We present optical and UV data on one such object, SN 2018gep, that displayed a fast rise with a mostly featureless blue continuum around peak, and evolved to develop broad features typical of an SN Ic-bl while retaining significant amounts of blue flux throughout its observations. This blue excess is most evident in its near-UV flux, which is over 4 mag brighter than other stripped-envelope supernovae, and is still visible in optical $g-r$ colors. Its fast rise time of $t_{\text{rise},V} = 5.6 \pm 0.5$ days puts it squarely in the emerging class of Fast Evolving Luminous Transients, or Fast Blue Optical Transients. With a peak absolute magnitude of $M_V = -19.53 \pm 0.23$ mag it is on the extreme end of both the rise time and peak magnitude distribution for SNe Ic-bl. These observations are consistent with a simple SN Ic-bl model that has an additional form of energy injection at early times that drives the observed rapid, blue rise. We show that SN 2018gep and the literature SN iPTF16asu have similar photometric and spectroscopic properties and that they overall share many similarities with both SNe Ic-bl and Fast Evolving Transients. Based on our SN 2018gep host galaxy data we derive a number of properties, and we show that the derived host galaxy properties for both SN 2018gep and iPTF16asu are consistent with the SNe Ic-bl and gamma-ray burst/supernova sample while being on the extreme edge of the observed Fast Evolving Transient sample.

Unified Astronomy Thesaurus concepts: Core-collapse supernovae (304); Supernovae (1668); Transient sources (1851); Ultraviolet transient sources (1854); Time domain astronomy (2109)

Supporting material: data behind figure, machine-readable table

1. Introduction

As recent transient surveys have begun to detect an increasing number of transients (Shappee et al. 2014; Chambers et al. 2016; Bellm et al. 2019) due to an increase in both cadence and volume of sky covered, new types have been discovered as well as outlier objects in otherwise well-understood classes (Kasliwal et al. 2012). Broad-lined Type Ic (Ic-bl) supernovae (SNe) are a subclass of stripped-envelope supernovae (SESNe) that are canonically classified by a lack of H and He observed in their spectra (Ic SNe; Filippenko 1997; Gal-Yam 2017; Modjaz et al. 2019) and that have an observed Fe velocity of $\gtrsim 1.5 \times 10^4$ km s $^{-1}$ (Modjaz et al. 2016). While SNe Ic-bl constitute an intrinsically rare class of

SNe ($\sim 4\%$ of the SESN rate,¹⁸ Shivvers et al. 2017), the overall number of SNe Ic-bl has increased dramatically over the last few years (Bianco et al. 2014; Modjaz et al. 2016; Shivvers et al. 2019; Taddia et al. 2019). In general, they have a broader range of light-curve rise times, including very rapid rises, and more luminous peak magnitudes than other SESNe; thus, they have larger inferred ^{56}Ni masses and explosion energies (Cano 2013; Taddia et al. 2015; Prentice et al. 2016) than other SESNe. They are also the only class of SNe that are directly connected to long-duration gamma-ray bursts (GRBs, Woosley & Bloom 2006; Modjaz 2011; Cano et al. 2017) although not every SN Ic-bl is observed to be accompanied by

¹⁸ Note the caveat that this SN Ic-bl rate is based on only one object in the LOSS sample.

¹⁷ MTA CSFK Lendület Near-Field Cosmology Research Group.

a GRB. The question whether SNe Ic-bl without observed GRBs may have produced jets is hotly debated; e.g., Corsi et al. (2016) suggest based on their radio data (mostly upper limits) from a sample of PTF SNe Ic-bl that less than 85% of those SNe Ic-bl may have harbored off-axis GRBs (i.e., the GRBs occurred but were not directed toward our line of sight). That study assumed densities and GRB energies that only apply to some cosmological GRBs, but are not shared by the most common kind of low-luminosity GRB such as GRB 060218/SN 2006aj, which had a much lower radio luminosity (Soderberg et al. 2006) than classical GRBs and whose origin is debated. Now a picture is emerging in which the broad lines in SNe Ic-bl may be caused by a jet, even if seen off-axis, as suggested by the hydro plus radiative transfer models in Barnes et al. (2018) and as claimed for SN 2020bvc (Izzo et al. 2020, but see Ho et al. 2020), and in which SNe Ic-bl share the same low-metallicity environments as SN-GRBs (Modjaz et al. 2020), and thus the same kind of low-metallicity progenitor.

Rare, known sub-classes of SNe are not the only objects to have been discovered in the ever-increasing data volume of transients. Recent discoveries of optical transients that evolve on the \sim 1–2 week timescales with luminosities comparable to that of SNe have been discovered (for recent reviews, see, e.g., Inserra 2019; Modjaz et al. 2019). Called variously “Rapidly Evolving Luminous Transients” (Drout et al. 2014), “Rapidly Rising Luminous Transients” (Arcavi et al. 2016), “Fast Evolving Luminous Transients” (Rest et al. 2018), “Rapidly Evolving Transients” (Pursiainen et al. 2018), and “Fast Blue Optical Transients” (FBOTs; Inserra 2019), they are an inhomogeneously observed class of objects whose progenitor systems and explosion mechanisms are unknown. The variety of names reflects the variety observed across the samples—some transients (e.g., Arcavi et al. 2016; Pursiainen et al. 2018) have a variety of colors and are not strictly blue but do evolve rapidly. Some samples consist strictly of more luminous objects (Arcavi et al. 2016) while others have a broader range of luminosities (Drout et al. 2014; Pursiainen et al. 2018). Potential explanations for these transient events have included magnetar-powered explosions, an explosive shock running into a dense circumstellar medium (CSM), off-axis GRB afterglows, black hole formation in a failed supernova, and the birth of binary neutron-star systems. Studies suggest that they are not *intrinsically* rare, with a rate of \sim 5%–10% of the core-collapse SN rate (Drout et al. 2014), but that the detection efficiency in most transient surveys are low due to these transients being sparsely sampled in a \sim 3 day cadence.

Here we present observations of SN 2018gep, which was spectroscopically identified as an SNe Ic-bl by discovery teams (Section 2.1) but, as we show, exhibits some features that are different from those of typical SNe Ic-bl and similar to those of rapidly evolving transients. In Section 2 we discuss our photometric and spectroscopic observations of this object. In Section 3 we discuss its photometric properties in comparison to others in the class of SN Ic-bl and others in similar regions of the transient rise-time versus peak magnitude parameter space. In Section 4 we examine our spectra of SN 2018gep and compare them to those of other objects. In Section 5 we discuss our spectroscopic long-slit and Integral Field Unit (IFU) studies of its host galaxy. In Section 6 we discuss the implications of SN 2018gep for understanding both SNe Ic-bl and Fast Evolving Transients.

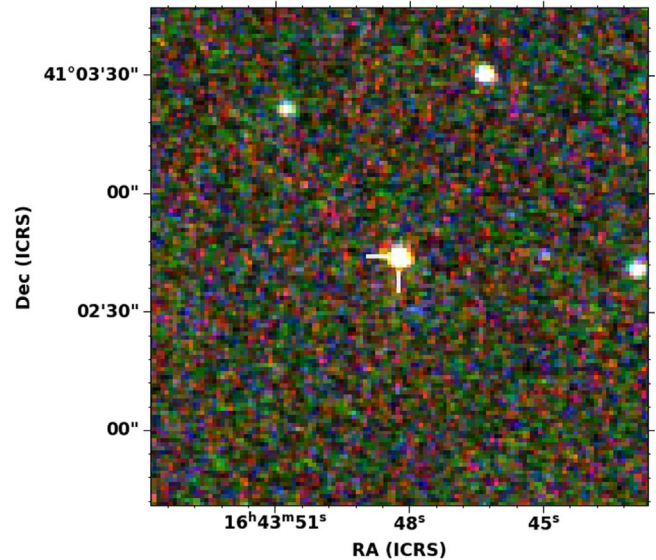


Figure 1. Swift $u/b/v$ composite color image of SN 2018gep and its host galaxy \sim 7 days after peak. The SN and host are blended as the point-spread function is similar in size to the host galaxy size.

2. Observations

2.1. Discovery and Classification

SN 2018gep/ZTF18abukavn (Figure 1, top) was first discovered on UT 03:55:17 2018 September 9¹⁹ (JD = 2458370.6634) by Ho et al. (2018) as part of the partnership ZTF survey (Bellm et al. 2019) at (R.A., decl.) = (16:43:48.22, +41:02:43.37). Initially the spectrum of SN 2018gep was characterized by a blue, mostly featureless continuum that evolved (see Section 4 and Ho et al. 2019a) until approximately 10 days later on 2018 September 19. Burke et al. (2018), as part of the Global Supernova Project (GSP), obtained an optical spectrum (see Section 2.3) and classified the object as a broad-line Type Ic supernova (Ic-bl) with an ejecta velocity of \sim 24,000 km s $^{-1}$ and a redshift of 0.032 which is consistent with the probable host galaxy identified by Ho et al. (2018), SDSS J164348.22+410243.3 with a $z = 0.033$ with an SN–host separation of \sim 1.5''.

2.2. Photometry

The ZTF public survey observed SN 2018gep between 2018 September 8 and 28 in the r -ZTF and g -ZTF filters. ZTF data were obtained from public alerts made available by the Las Cumbres Observatory MARS broker, which provides access to the publicly available background subtracted ZTF data products.

The GSP obtained additional Las Cumbres Observatory (LCO) $BVgri$ -band follow-up data with the Sinistro and Spectral cameras on 1 m and 2 m telescopes, respectively. Using `lcogtsnpipe` (Valenti et al. 2016), a PyRAF-based photometric reduction pipeline, point-spread function (PSF) fitting was performed. Reference images were obtained with the Sinistro and Spectral Imager after the SN faded and image subtraction was performed using PyZOGY (Guevel & Hosseinzadeh 2017), an implementation in Python of the subtraction algorithm described in Zackay et al. (2016). BV -band data were calibrated to Vega magnitudes using the

¹⁹ UT will be used as a reference timezone throughout this paper.

AAVSO Photometric All-Sky Survey (Henden et al. 2009), while *gri*-band data were calibrated to AB magnitudes using the Sloan Digital Sky Survey (SDSS, Aguado et al. 2019). Science observations were taken between 2018 September 22 and 2018 October 30 with template photometry taken between 2019 January 22 and 26.

Additional photometric observations were collected with the 0.6/0.9 m Schmidt telescope at Piszkésteto Mountain Station of Konkoly Observatory, Hungary, using the $4k \times 4k$ FLI CCD equipped with Johnson–Cousins–Bessel *BVRI* filters. After the usual bias, dark, and flatfield corrections, PSF photometry was performed on the SN and a set of nearby stars used as tertiary standards. Photometric calibration was done using PS1 photometry on the local tertiary standards, after transforming the cataloged g_P , r_P , i_P magnitudes to *BVRI* ones via the calibration by Tonry et al. (2012). Finally, the flux contribution from the host galaxy was taken into account by computing aperture photometry on the host as it appeared on the PS1 frames and subtracting its fluxes from those obtained from PSF photometry on the Konkoly frames.

Observations with the Neil Gehrels Swift Observatory (Swift hereafter; Gehrels et al. 2004) Ultra-Violet/Optical Telescope (Roming et al. 2005) began on 14:02:56 2018 September 9 (~ 0.5 day after discovery) using three optical (u , b , v) and three UV filters ($uvw2$, $uvm2$, $uvw1$: $\lambda_c = 1928, 2246, 2600$ Å, respectively; Poole et al. 2008) after being triggered by Schulze et al. (2018) and Ho et al. (2019a). Regular observations continued through 2018 October 3 with a final observation obtained on 2018 October 29. Data were reduced using the process described in Pritchard et al. (2014) with the final observation used for galaxy template subtraction. While there may be some small contamination from the SN at this time, any UV emission is far below the Swift sensitivity at this time frame and the optical observations from Swift are consistent with the other sources presented here (LCO, Konkoly). Data from these sources are presented in Figure 2 and made available in Table 1.

2.3. Spectroscopy

We obtained optical spectroscopy of the SN as well as its host galaxy and list the journal of our spectroscopic observations in Table 2.

Additional observations of the location of SN 2018gep and its host galaxy were obtained by two different telescopes at 1.5–2 months after the explosion. One was obtained via Director’s Discretionary Time (PI: Bensch) using the Potsdam MultiAperture Spectrophotometer (PMAS; Roth et al. 2005), which is an IFU instrument, mounted on the 3.5 m telescope at the Centro Astronómico Hispano en Andalucía (CAHA). The other was with the Low-Resolution Imaging Spectrometer (LRIS, Oke et al. 1995; McCarthy et al. 1998; Rockosi et al. 2010) at the 10 m W. M. Keck Observatory on Maunakea, Hawaii, as part of the LCO–GSP follow-up program (PI: Valenti), using a long-slit aperture.

The IFU observations using the PMAS instrument in PPak mode (Verheijen et al. 2004; Kelz et al. 2006) were carried out on 2018 November 7. We used the V500 grating with $G_{\text{rot}} = 143.5$, which covers a wavelength range between ~ 3750 and 7500 Å at a resolution of 6.5 Å FWHM, corresponding to ~ 350 km s $^{-1}$. The PPak IFU consists of 331 science fibers with diameters of 2.7 ”. The science fibers are placed in a hexagonal parcel resulting in a filling factor of 65%, and cover a field-of-view (FOV) of $72'' \times 64''$. For sky subtraction 36 sky fibers are placed around the science fibers. An additional 15 fibers illuminated by internal

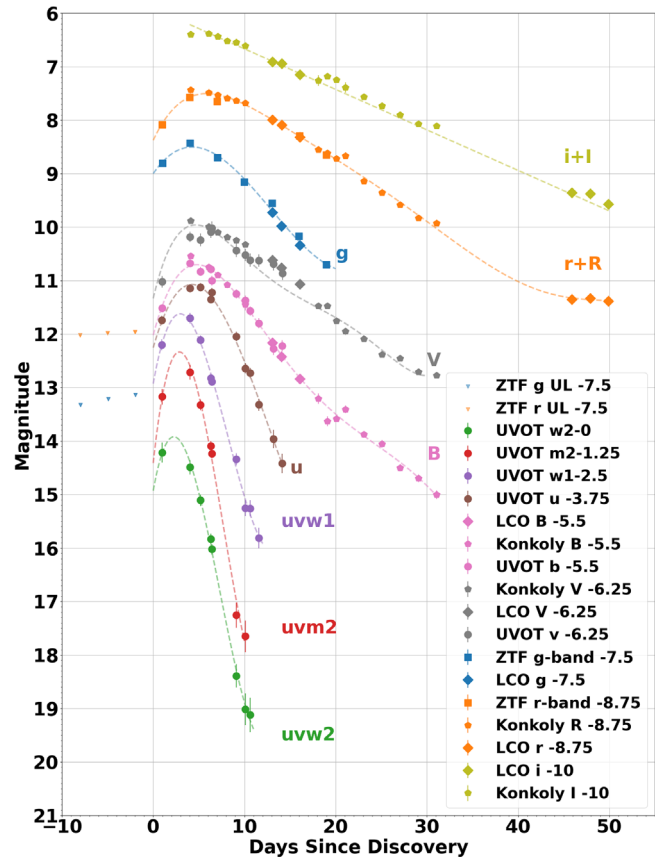


Figure 2. Multi-color photometry (and upper limits) of SN 2018gep. The lines are low-order polynomial lines fit to the data purely for visual clarity.

Table 1
Photometry of SN 2018gep

JD	mag	mag _{err}	Instrument	Filters
2458383.7278	17.665	0.0194	LCO 2m0-01	<i>B</i>
2458383.7326	16.864	0.0154	LCO 2m0-01	<i>V</i>
2458383.7376	17.230	0.0089	LCO 2m0-01	<i>g</i>
2458383.7412	16.741	0.0262	LCO 2m0-01	<i>r</i>
2458383.7445	16.909	0.0143	LCO 2m0-01	<i>i</i>

(This table is available in its entirety in machine-readable form.)

lamps are used to calibrate the instrument. Three science exposures of 1200 s each were obtained at a signal-to-noise ratio (S/N) of ~ 10 per angstrom for the spectral continuum. We used a dithering pattern consisting of three pointings to cover the entire FOV including the spaces in-between the fibers. In Figure 3 (bottom) we show the FOV of the PPak IFU and the region around the host which is plotted in the subsequent figures that display host-galaxy properties.

To reduce the PMAS–PPak data we used a python-based pipeline that executes the following steps: identification of the position of the spectra on the detector along the dispersion axis; extraction of each individual spectrum; distortion correction of the extracted spectra; wavelength calibration; fiber-to-fiber transmission correction; flux-calibration; sky-subtraction; cube reconstruction; finally, differential atmospheric correction (for more details, see García-Benito et al. 2010, 2015; Husemann et al. 2013). These IFU data and their analysis are discussed as part of our host-galaxy study in Section 5.

Table 2
Spectroscopic Observations of SN 2018gep and Its Host Galaxy

UT Date	JD	$t_{V,\max}^{\text{a}}$ (days)	Tel. + Instr.	Wave. Range (Å)	P.A. (°)	Airmass	Slit ($''$)	Exp. (s)
2018-09-11.31	2458372.81	-3.7	OGG 2m+FLOYDS	3700–10000	95.3	1.74	2.0	1800
2018-09-19.24	2458380.74	+4.3	OGG 2m+FLOYDS	3700–10000	112.6	1.30	2.0	1800
2018-11-07.45 ^b	2458429.95	+54.5	CAHA+PMAS ^c	3750–7500	N/A	2.2	N/A	3×1200
2019-02-05.64 ^b	2458520.14	+144.6	Keck+LRIS	3200–9200	250	1.33	1.0	900

Notes.

^a Days with respect to V-band maximum. Note that SN 2018gep's rise time in the V-band is $t_{\text{rise},V} = 5.6 \pm 0.5$ days (see Section 3), such that our first two spectra were taken 1.9 and 9.9 days after the presumed date of explosion, respectively.

^b No SN light, only host galaxy.

^c IFU observations, thus long-slit information such as slit size and P.A. is not applicable here.

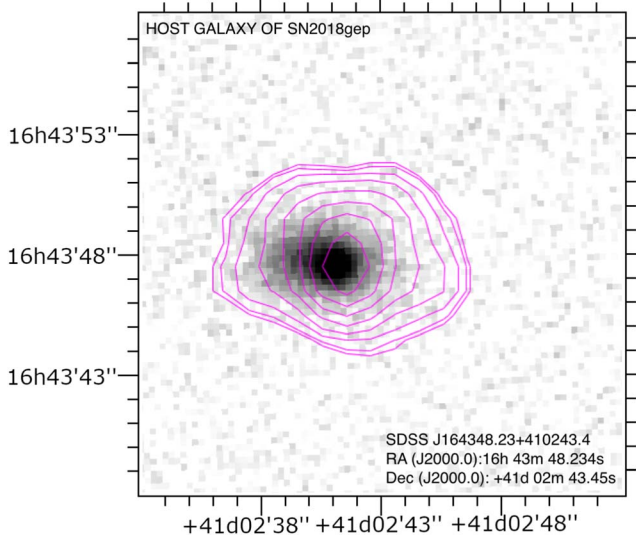


Figure 3. PanSTARRS-1 g' image with contours that are equivalent to a g' -band image that we extracted from the IFU data—see Section 5 for more details.

The late-time long-slit Keck spectrum (see Table 2) was reduced in the standard way using the LPIPE pipeline (Perley 2019)—no SN emission was detected at the location of SN 2018gep in either the 1D or the 2D spectra. The spectrum is included as part of our host-galaxy study in Section 5.

3. Light Curve Analysis

3.1. Rise Time and Absolute Magnitude Comparison

The combined UV-optical light curves for SN 2018gep are shown in Figure 2. From the Swift v -band data we calculate that the epoch of maximum light in the v -band is $t_{\text{peak},V} = 58375.7 \pm 0.8$ MJD using the Monte Carlo method outlined in Bianco et al. (2014). Using the same method we calculate the observed peak magnitude in the r -band, $m_{r,\text{peak}} = 16.29 \pm 0.03$ mag. The relatively deep upper limits from the ZTF survey provide for a strong constraint on the rise time—using the last ZTF upper limit (Ho et al. 2019a) as an upper limit on the explosion date we calculate a rise time of $t_{\text{rise},V} = 5.6 \pm 0.5$ days and $t_{\text{rise},r} = 5.1 \pm 0.5$ days. From the observed redshift of $z = 0.031875 \pm 0.000075$ (see Section 5) we calculate the absolute magnitude for SN 2018gep at peak to be $M_V = -19.53 \pm 0.23$ mag and $M_r = -19.54 \pm 0.24$ mag using the astropy (Astropy Collaboration et al. 2013; Price-Whelan et al. 2018) cosmology package and a flat Λ CDM model with $H_0 = 74.22 \text{ km s}^{-1} \text{ Mpc}^{-1}$ (Riess et al. 2019) and $\Omega_m = 0.286$, and

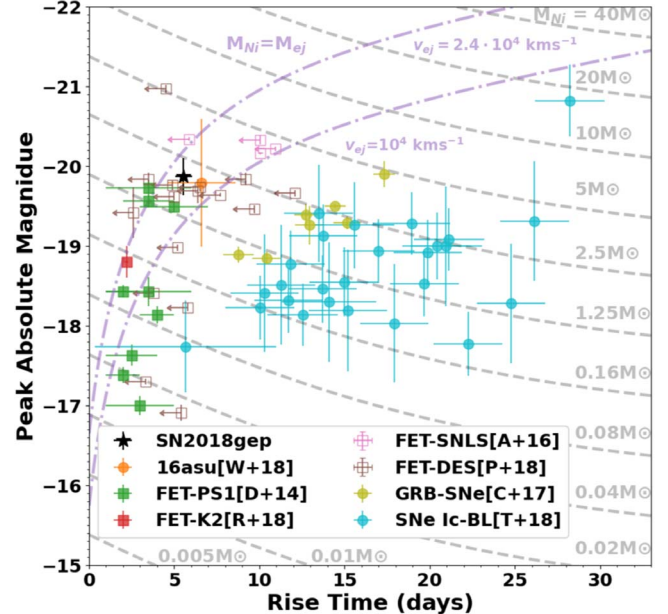


Figure 4. Rest frame rise time vs. peak magnitude for a variety of transient sources. The PTF/iPTF SNe Ic-bl without observed gamma-ray bursts (GRBs) (T+19; Taddia et al. 2019) cluster around the GRB/SNe (C+17; Cano et al. 2017) with a small gap in rise time between most of the sample (PTF10vgy has some overlap; see Figure 5) and the Fast Evolving Transients (D+14, A+16, P+18, R+18; Drout et al. 2014; Arcavi et al. 2016; Pursiainen et al. 2018; Rest et al. 2018). The values plotted for SN 2018gep are for our r' -band data. The SN Ic-bl that occupies a similar position as SN 2018gep in this phase space is iPTF16asu (W+18, T+19; Whitesides et al. 2017; Taddia et al. 2019), which is discussed in more detail in Section 3.

corrected for Milky Way line-of-sight extinction using the values from Green et al. (2019). This cosmology model is used throughout the rest of this work for consistency.

Assuming an SN is powered by the typical ^{56}Ni -decay model, for a particular absolute magnitude and SN rise time, we may calculate an ejecta mass and nickel fraction as outlined in Arcavi et al. (2016) (Equations (1) and (2) and following from Arnett 1982; Stritzinger & Leibundgut 2005; Wheeler et al. 2015). It is important to note that this approach makes a number of simplifying assumptions including: spherical symmetry, a constant opacity, a central nickel concentration, that the photospheric velocity is characteristic of the ejecta velocity, and optical to bolometric corrections for both the rise-time and peak absolute magnitude. This relation is therefore more indicative than strict, and in Figure 4 we sketch out lines for a series of ejecta masses

and two additional lines corresponding to objects in which the ejecta mass must be entirely composed of nickel to power their light curve. If an object lies above these lines, an additional source of energy injection or a different source of power is required. Since this limit also depends on ejecta velocity, we draw two lines: the lower line corresponding to a typical SN with $\sim 10,000 \text{ km s}^{-1}$ expansion and the top line corresponding to an SN with $\sim 24,000 \text{ km s}^{-1}$ expansion velocity as measured from the post-maximum spectrum of SN 2018gep. In this parameter space, SN2018gep is like the other luminous fast-rising transients shown, namely right on the border of what can be easily described with simple nickel-powered relations, and it is consistent with being an outlier from the other SNe Ic-bl which are comfortably below this relation. This implies that SN 2018gep most likely had to have an additional powering source besides the decay of ^{56}Ni (see also Ho et al. 2019a for a detailed model involving CSM interaction and pre-explosion mass loss).

3.2. Light Curve and Color Comparison with Other SNe Ic-bl

In Figure 5 we compare the light curve of SN 2018gep to a sample of SNe Ic-bl from Taddia et al. (2019) in the optical and a few select SESNe with Swift UV observations. The optical evolution of SN 2018gep is broadly similar to the most rapidly evolving SNe Ic-bl. The most similar objects are iPTF16asu (an outlier as noted in Taddia et al. 2019), PTF10vgy (Corsi et al. 2012), and SN 2006aj. While the optical evolution of SN 2018gep and iPTF16asu is similar to that of the SN Ic-bl population as a whole, the early color evolution is *not*, particularly in the UV and bluer filters. As we show in the middle and bottom panels of Figure 5, there is significantly more blue emission from these SNe at early times than from the rest of the Ic-bl sample, by more than a magnitude in the optical and almost 4 mag in the UV. By ~ 10 days after r -band maximum the color curve of SN 2018gep becomes similar to that of the sample as a whole, albeit remaining somewhat on the blue side. *Only SN 2018gep and iPTF16asu show this significant early blue excess.* PTF10vgy and SN 2006aj have similar colors to the SNe Ic-bl sample as a whole. The only other similarly blue emission is that from SN 2006aj at early times, but it has a significantly faster evolution. The mechanism that drives this is still a topic of some debate (see Irwin & Chevalier 2016 for a discussion), and the SN component of the GRB/SN SN2006aj quickly returns to the “typical” behavior of the SNe Ic-bl sample as a whole—including during phases where SN 2018gep is still UV bright.

3.3. Comparison with PS1 Fast-evolving Transients

In Sections 3.1 and 3.2 we show that while SN 2018gep shares similarities with other Ic-bl SNe, it is a notable outlier in terms of color, absolute magnitude, and rise time. In Section 3.1 we show that other objects that may behave similarly to SN 2018gep are the recently discovered class of Fast Evolving Transients first noted by Drout et al. (2014) and later in Arcavi et al. (2016), Rest et al. (2018), and Pursiainen et al. (2018). With many of these objects having poorly constrained rise times due to their rapid evolution, we focus on a comparison with the PS1 sample from Drout et al. (2014) which has a significant number of objects with a detected rise as well as multi-color observations. These are, however, found at a significantly large range of redshifts ($z = 0.07\text{--}0.65$); to compare we match the observed SN 2018gep band with the closest rest-frame band of a PS1 object, as shown in Figure 6.

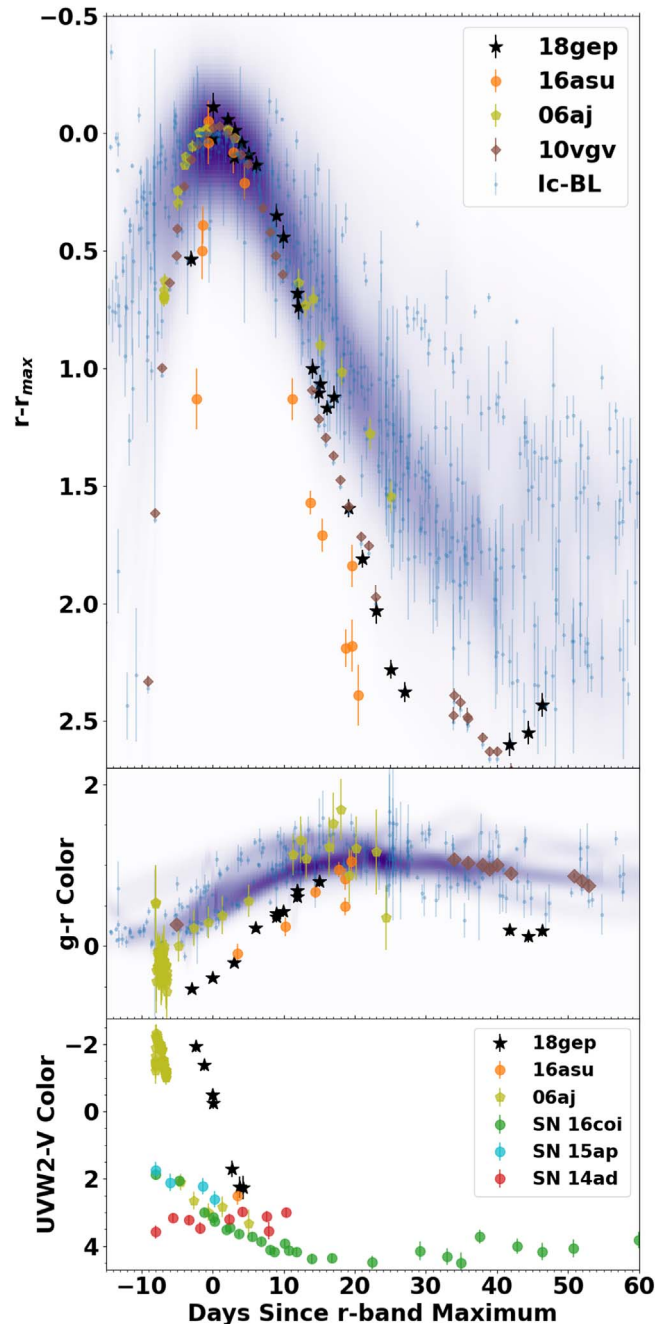


Figure 5. Comparison of SN 2018gep with other SNe Ic-bl in the optical (top, middle; Taddia et al. 2019) and UV. When compared to the Taddia et al. (2019) SN Ic-bl sample in the rest frame, the decline rate of SN 2018gep is similar to the fastest in that sample (including iPTF16asu), and is significantly more blue at early times than the rest of the sample. This is even more apparent when we compare the UV emission observed with Swift, and the only other Ic-bl SNe with similar emission is the early-time emission (either shock cooling or GRB) from GRB 060218/SN 2006aj (Campana et al. 2006). At late times the observed colors of SN 2018gep return to the blue side of the standard SN Ic-bl distribution.

This is a rather coarse measurement, as the relative filter bandpass is different and a more detailed analysis would perform k -corrections to address this. However, we choose to avoid k -corrections as they are spectral energy distribution (SED) dependent and we have limited information about the SEDs of all PS1 objects, while we know that they undergo significant color evolution.

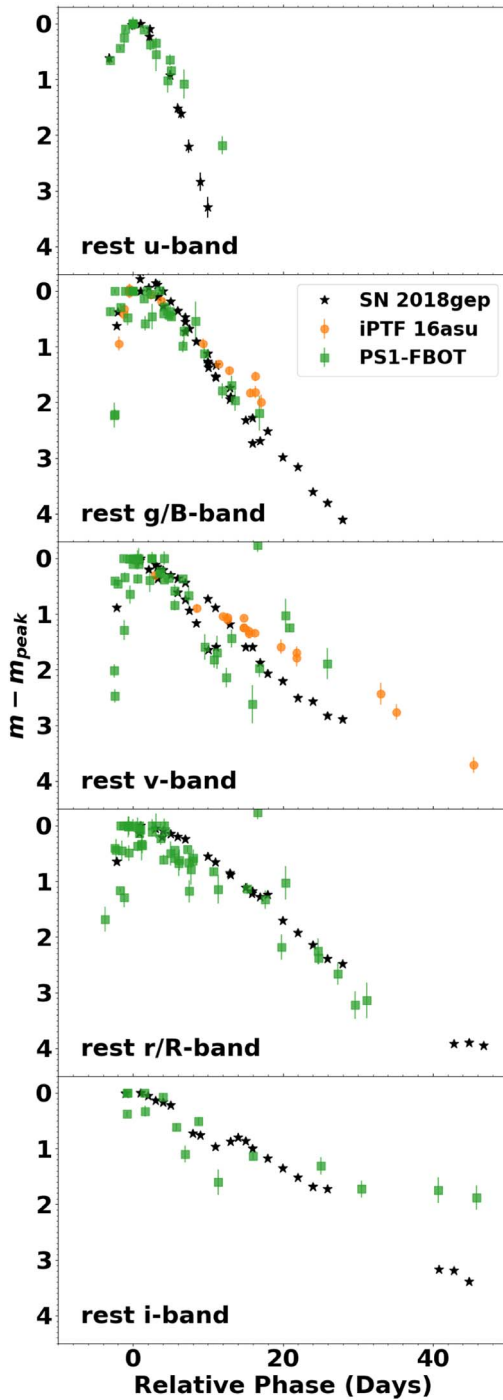


Figure 6. Comparison of SN 2018gep with PS1 Fast Evolving Transient gold and silver samples from Drout et al. (2014). Filters have been matched by using the closest rest-frame central wavelength with time dilation but no k -corrections have been applied, implying a qualitative comparison only. Given the differing band passes and spectral coverage the overall light curve shape between the Fast Evolving Transients and SN 2018gep is similar. Some significant scatter may be seen in the rest V -band around 15–20 days and some deviation at late times in some objects in the rest u -band and rest i -band.

As seen in Figure 6, both SN 2018gep and iPTF16asu have similar relative light curve shapes as the PS1 Fast Evolving Transient population as a whole. Furthermore, the observed $g-r$ colors are similar to the sample as reported in Drout et al. (2014). There is some suggestion that there may be some longer-lived emission in some PS1 fast transients (as seen in

the late-time rest-frame i -band comparison and u -band comparison), although these late-time deviations each come from a single PS1 object and it is not clear how homogeneous a sample these objects is.

While the high luminosity of SN 2018gep ($M_V = -19.53 \pm 0.23$ mag and $M_r = -19.54 \pm 0.24$ mag) may lie close to that of superluminous SNe (SLSNe), which appear to range from $-22 \lesssim M_g \lesssim -20$ mag (De Cia et al. 2018; Lunnan et al. 2018; Kann et al. 2019), its light curve is distinctly different: The “fast” SLSNe-Ic have typical rise times of ~ 28 days (Inserra 2019), namely ~ 4 –5 times larger than for SN 2018gep. Furthermore, while they may rise as quickly as in ~ 15 days (Inserra 2019), SLSNe (both fast and slow) tend to decline slower by a factor of 2 compared to their rise time (Nicholl et al. 2015; De Cia et al. 2018), which is a trait not seen in SN 2018gep specifically, nor FBOTS in general (Drout et al. 2014).

4. Spectroscopic Analysis

The spectra of SNe are crucial diagnostics which reveal the elemental composition and dynamics of the ejecta. Since there are relatively few FBOTS with spectra, here we present a detailed analysis of our two spectra of SN 2018gep and their comparison to SN population spectra as well as to individual SN spectra. Our two medium-resolution optical spectra of SN 2018gep at phases $t_{V_{\max}} = -3.7$ and $t_{V_{\max}} = 4.3$ days relative to V -band maximum are shown in Figure 7. The early spectrum, taken just before maximum light and around 2 days after the assumed date of explosion is characterized by a strong, featureless blue continuum, with a single absorption feature at around 4050 Å that may be due to blended transitions of highly ionized carbon (see Ho et al. 2019a). The later spectrum at phase $t_{V_{\max}} = 4.3$ days displays broad features typical of an SN Ic-bl spectrum.²⁰ For the post-maximum spectrum, we calculate the absorption and line-width velocities for the Fe II 5169 Å absorption feature using the techniques from Modjaz et al. (2016) and find an absorption velocity $v_{\text{abs}} = 23800 \pm 2200 \text{ km s}^{-1}$ and a width velocity $v_{\text{lw}} = 10100^{+300}_{-500} \text{ km s}^{-1}$. This high absorption velocity is consistent with SN Ic-bl events associated with GRBs (see Figure 7; Modjaz et al. 2016).

In order to evaluate the spectroscopic similarities between SN 2018gep and other SNe, we used the SNID code (Blondin & Tonry 2007) to match SN 2018gep to other stripped-envelope SNe, whose SNID templates have been produced by Liu et al. (2016), Modjaz et al. (2016), Liu et al. (2017), and Williamson et al. (2019). Table 3 shows the top five SNID matches for the $t_{V_{\max}} = 4.3$ day spectrum of SN 2018gep, along with the SNID r_{lap} value, which is the indicator of the fit. SNID cannot match the earliest spectrum due to the relative lack of SN features combined with the scarcity of pre-maximum observed spectra in the SNID template library. The majority of the SNID matches are SN Ic-bl spectra, but SNID calculates matches on the continuum-removed spectra. Therefore, the SNID matches only reflect spectral behavior in the absorption lines, with stronger absorption lines having higher weights.

In order to investigate the behavior of the continuum in SN 2018gep, we overplot in Figure 7 the mean spectra of SNe Ic-bl (from Modjaz et al. 2016) and those of SLSNe from Liu et al. (2017). SLSNe are included here since they also show broad lines

²⁰ The SN 2018gep spectra have very narrow H α and H β emission peaks, which are clearly due to the underlying host galaxy.

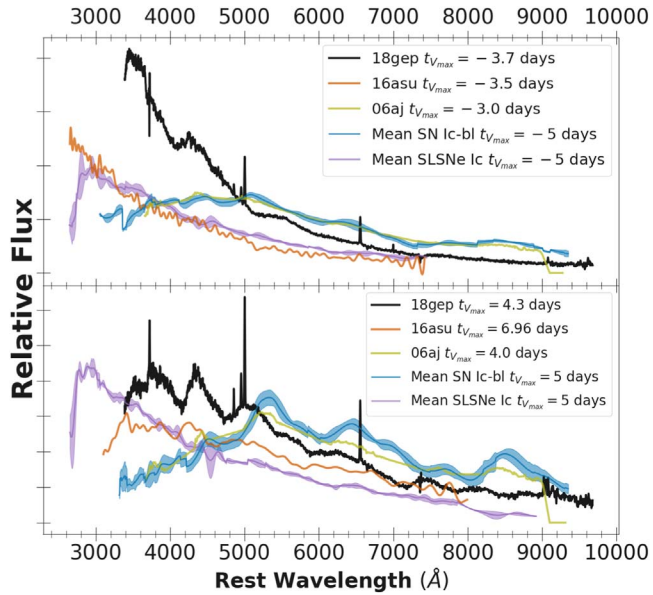


Figure 7. Comparison of SN 2018gep (black) spectra to mean (plus standard deviation) spectra of SNe Ic-bl (blue) and SLSNe Ic (purple) classes, along with direct comparisons to SN 2006aj (yellow) and iPTF16asu (orange). The excess blue flux in the SN 2018gep spectra compared to the mean SNe Ic-bl and even SLSNe Ic spectra, and that of iPTF16asu, is clearly evident. The SN 2018gep spectra are available in FITS format as the data behind the figure.

(The data used to create this figure are available.)

Table 3
SNID Matches to SN 2018gep at $t_{V\max} = 4.3$ Days

SN	Phase (days)	Classification	r_{lap}
2006aj	-0.2	Ic-bl	7.59
2003bg	-19.1	IIb-pec	6.11
2007uy	-6.3	Ib-pec	5.94
2016coi	-10.6	Ic-bl	5.82
2006aj	5.0	Ic-bl	5.78

Note. The top five SNID matches to the $t_{V\max} = 4.3$ days spectrum for SN 2018gep. Phase is measured relative to the date of V -band maximum. Both SN 2003bg and SN 2007uy exhibited broad lines at early times, in particular during their listed phases, which then disappeared over time (Mazzali et al. 2009; Modjaz et al. 2014). Thus, these two SNe are called peculiar for their type.

in their spectra (Liu et al. 2016; Quimby et al. 2018), have blue colors (see Inserra 2019 for a recent review), and are also suggested to be driven by the CSM or magnetars, as we also do for SN 2018gep (see Section 6). In addition, we include the individual objects SN 2006aj (Modjaz et al. 2006, 2014) and iPTF16asu (Whitesides et al. 2017) since they have some similarities to SN 2018gep. At early times, SN 2018gep is distinguished from both SNe Ic-bl and SLSNe Ic spectra by its strong blue continuum. In addition, we can see clearly from the spectra that SN 2018gep is even bluer than iPTF16asu—especially pre-maximum—something that could not be discerned from the photometry given the lack of pre-maximum g -band and Swift data for iPTF16asu (note that the y -axis uses relative flux, so differences in color manifest as differences in the overall shape and slope of the spectra). At later times ($t_{V\max} = 4.3$ days), SN 2018gep resembles the mean SN Ic-bl spectrum and SN 2006aj spectrum for $\lambda > 5000 \text{ \AA}$, but there is clear excess

flux in the blue part of the SN 2018gep spectrum, which is consistent with our analysis of the SN 2018gep light curve in Figure 5. At wavelengths $\lambda < 5000 \text{ \AA}$, the lines in SN 2018gep closely resemble those in iPTF16asu, but its continuum is bluer than that of iPTF16asu. This blue flux excess could be due to interaction with the CSM or due to a hotter underlying photosphere (Ho et al. 2019a). The color of SN 2018gep is more similar to that of SLSNe Ic after maximum than it was pre-maximum. It is difficult to compare the spectra of SN 2018gep to those of Fast Evolving Transients due to the relative lack of spectra, i.e., small number statistics. For example, in the PanSTARRS sample, six out of 10 Fast Evolving Transients had spectra, none of which was pre-maximum. Of those objects with post-maximum spectra, only two to three had spectra where one could have detected SN Ic bl-like lines similar to those of SN 2018gep, and no such broad lines were detected.

For the SLSN comparison, we note that one characteristic spectroscopic feature of SLSNe Ic is the “W” feature in early-time spectra of SLSNe (Quimby et al. 2011, 2018; Mazzali et al. 2016; Liu et al. 2017; Gal-Yam 2019). While we do not detect this feature in our pre-max spectrum (which is 2 days after explosion), it was observed by Ho et al. (2019a) in their spectrum 4 days after explosion. Thus SN 2018gep did show this SLSN-like spectroscopic absorption feature, though other SESNe have shown it too, such as SN 2008D (Modjaz et al. 2009).

In summary, our detailed spectral analysis shows that SN 2018gep has lines very similar to those in SNe Ic-bl (in terms of absorption and width velocities), but a much bluer continuum than SNe Ic-bl and iPTF16asu, both before and after maximum light. In addition, before maximum light, the spectrum of SN 2018gep appears to be even bluer than the mean spectrum of SLSNe.

5. Host Galaxy Analysis

Here we analyze in detail the host galaxy of SN 2018gep and compare it to those of other SN samples (including well-understood ones) and the general population of star-forming galaxies in order to understand its explosion conditions and progenitor.

The study of the host galaxy environment of a transient in order to constrain the progenitor of the particular transient has a rich history (e.g., Modjaz et al. 2008, 2020; Thöne et al. 2019; for a review see Anderson et al. 2015), and is an emerging field for the new kind of transients being discovered by innovative surveys, such as FBOTs. Historically this has been done with long-slit spectroscopy; however, recent advances in the instrumentation of IFUs and large samples of nearby SNe from ongoing surveys have allowed these studies to be done with IFUs to allow for increased resolution around the SN site and better resolution of the host galaxy and its associated dynamics (see Kuncarayakti et al. 2013a, 2013b, 2018; Galbany et al. 2014, 2016, 2018 for a more general discussion across SNe sub-types).

5.1. IFU Data

This study represents the first IFU host-galaxy study of a Fast Evolving Transient. The PPak IFU spaxels in our final cube have an angular size of $1'' \times 1''$; however, the seeing during observations was only $1''.8$, hence the nominal spatial resolution is lower. For our spatially resolved analysis of the

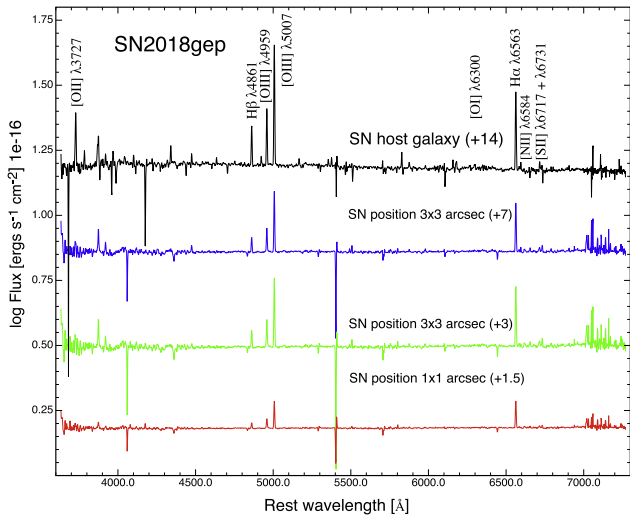


Figure 8. Integrated spectra extracted from the PMAS data cube: the entire galaxy (black) and regions around the SN position using an area of $1'' \times 1''$ (red), $3'' \times 3''$ (five spaxels, green) and $3'' \times 3''$ (nine spaxels, blue) and are offset for readability. The strong, narrow absorption lines are residuals from sky line subtraction.

host galaxy we use custom-written IDL codes to extract emission-line maps and properties from the data cubes.

5.1.1. Emission-line Analysis

In order to obtain emission-line fluxes in each spaxel we sum the fluxes in the spectral direction around the redshifted position of each emission line and subtract the galaxy continuum. 2D maps of the main emission lines are shown in the Appendix, Figure 13. To study the properties of the region around the SN at different spatial resolutions, we extract 1D spectra from 1, 5, and 7 spaxels centered on the SN position using QFitsView.²¹ The spectra are shown in Figure 8

Using the integrated spectrum of the host galaxy we determine a precise redshift from the strong emission lines of $\text{H}\beta$ $\lambda 4861 \text{ Å}$, $[\text{O III}] \lambda 4959 \text{ Å}$, $[\text{O III}] \lambda 5007 \text{ Å}$, $[\text{O I}] \lambda 6300 \text{ Å}$, $\text{H}\alpha \lambda 6563 \text{ Å}$. The mean value obtained from all emission lines yields $z = 0.031875 \pm 0.000075$.

To obtain the interstellar extinction in the host galaxy, we use the Balmer decrement of $\text{H}\alpha/\text{H}\beta$ according to Domínguez et al. (2013), adopting the Calzetti et al. (2000) attenuation curve with $R_V = 4.05$ which assumes a starburst attenuation law. We assume the standard recombination model for star-forming galaxies and Case B for H I recombination lines (Osterbrock & Ferland 2006). The intrinsic Balmer decrement at an electron temperature $T = 10^4 \text{ K}$ and density $n_e = 10^2 \text{ cm}^{-3}$, is expected to be $j_{\text{H}\alpha}/j_{\text{H}\beta} = 2.86$. The values obtained for the reddening in the galaxy and the regions around the SN are listed in Table 4. The distribution of the extinction across the galaxy is shown in Figure 9. Curiously, the spectra of the SN line-of-sight region indicate some extinction while the extinction based on the integrated spectrum of the host is consistent with zero. As we increase the aperture of extraction from the SN position (see Table 4) we see the calculated extinction drop until for the total host-galaxy-integrated IFU spectrum the overall extinction is low and consistent with $E(B - V) = 0 \text{ mag}$. This is also consistent with the zero to low value obtained from the Keck LRIS host-galaxy spectrum. One

explanation for this apparent discrepancy may be that the overall galaxy emission has little extinction and, while extinction is present throughout the galaxy it is not homogeneously distributed. Therefore the integrated spectrum is dominated by regions with little extinction but more emission, explaining the overall low $E(B - V)$. This is reflected in the IFU map in Figure 9 which shows that the distribution of the extinction is not uniform. We observe that the high extinction in the SN line-of-sight region could either imply a considerable amount of dust at the SN site or it is dust behind the SN. The latter is favored by the fact that the SN is observed to be UV bright, ~ 4 mag bluer in the UV than other SNe Ic-bl at early times. If we de-reddened the SN data using extinction values based on the $1'' \times 1''$ section around the SN in the IFU map ($E(B - V) = 0.5 - 0.6 \text{ mag}$, $A_V = 1.8 \text{ mag}$) the intrinsic peak luminosity in the UV would be unreasonably large. We therefore conclude that if there is dust, it is located behind the SN, hence not showing up in the NaD absorption in the sightline but can affect the Balmer decrement measured from the projection of the excited gas at and around the SN site.

The emission-line fluxes of the spectra were measured using SPLIT in IRAF. Statistical errors were calculated following Pérez-Montero & Díaz (2003). We found an offset between the SDSS photometry and the magnitude derived from the integrated spectra of $m - m_0 = 0.26 \text{ mag}$ and therefore calibrated the emission-line fluxes using the SDSS g' and r' filters. Fluxes were corrected for Galactic extinction ($A_v = 0.0286 \text{ mag}$), and extinction in the host galaxy as estimated in each corresponding spectrum. We list the final extinction-corrected, SDSS-calibrated emission-line values as extracted for different parts of the galaxy in Table 4 and the Appendix.

5.1.2. Derived Host Properties

The luminosity of the $\text{H}\alpha$ nebular line serves as the tracer of the star formation rate (SFR). To calculate the SFR we follow the relations in Kennicutt & Tamblyn (1994) assuming $T = 10^4 \text{ K}$ and Case B recombination. The values of $L(\text{H}\alpha)$ and the SFR for both the host galaxy and the SN region are listed in Table 4. The SFR distribution in the galaxy is shown in Figure 9. The SFR at the SN site is 1/10 to 1/2 of that of the overall host galaxy, depending on the size of the spaxel extraction region in the IFU data (see Table 4).

To determine metallicities (Z) we use the Python code pyMCZ (Bianco et al. 2016), which calculates oxygen abundances using strong-emission-line standard metallicity diagnostics based on a Monte Carlo method to derive the statistical oxygen abundance confidence region. Various emission-line ratios are used in up to 15 theoretical/empirical/combined metallicity calibrations implemented in the code. We present the combination of the emission lines used in each calibration and the results in Table 5 and refer the reader to the references listed in Table 5 for a more detailed discussion on the individual diagnostics. Due to its low S/N we decided to exclude $[\text{O II}] \lambda 3727 \text{ Å}$ from the metallicity measurements. Our results show no significant difference between the metallicity of the SN region and the integrated host-galaxy value.

Figure 9 shows distributions of metallicities across the galaxy using the calibration of Marino et al. (2013). Metallicities for other calibrators are shown in the Appendix for comparison.

²¹ <http://www.mpe.mpg.de/~ott/QFitsView>

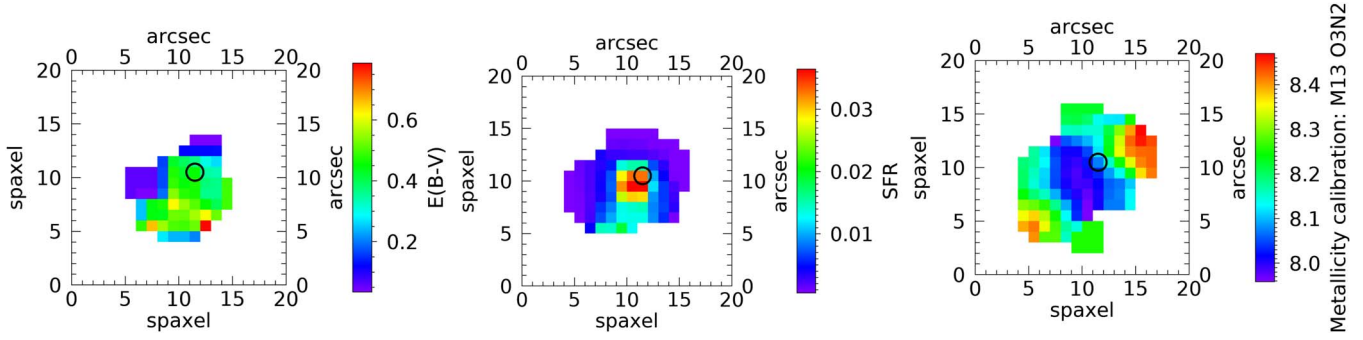


Figure 9. Maps of extinction (left), star formation rate (middle) and metallicity (right) using the O3N2 parameter in the calibration of Marino et al. (2013). The black circle indicates the position of SN 2018gep.

Table 4
Emission-line Fluxes Corrected for Galactic and Host-galaxy Extinction, and Calibrated with SDSS Photometry

Emission Line	λ (Å)	Host Galaxy	λ (Å)	SN Region $1'' \times 1''$	λ (Å)	SN Region $3'' \times 3''$ (five spaxels)	λ (Å)	SN Region $3'' \times 3''$ (nine spaxels)
[O II] $\lambda 3727$ Å	3727.929	57.705 ± 1.249	3725.427	7.208 ± 2.241	3725.927	23.161 ± 4.500	3726.198	19.215 ± 3.995
H β $\lambda 4861$ Å	4861.477	36.445 ± 0.547	4861.556	3.649 ± 0.640	4861.404	14.952 ± 1.952	4861.405	16.402 ± 2.172
[O III] $\lambda 4959$ Å	4959.094	54.767 ± 0.612	4959.239	6.105 ± 1.030	4959.112	25.487 ± 3.214	4959.088	26.438 ± 3.385
[O III] $\lambda 5007$ Å	5007.047	155.614 ± 0.894	5007.136	16.767 ± 2.773	5007.057	73.183 ± 9.054	5007.027	76.130 ± 9.565
[O I] $\lambda 6300$ Å	6297.685	8.126 ± 0.704
H α $\lambda 6563$ Å	6562.696	84.348 ± 1.171	6562.640	10.326 ± 1.274	6562.660	42.315 ± 3.954	6562.650	46.437 ± 4.413
[N II] $\lambda 6584$ Å	6584.315	3.892 ± 0.584	6584.007	0.556 ± 0.096	6583.500	1.760 ± 0.309	6583.506	2.070 ± 0.445
[S II] $\lambda 6717$ Å	6716.741	7.075 ± 0.552	6714.937	1.790 ± 0.252	6714.704	4.303 ± 0.554	6714.525	5.982 ± 0.766
[S II] $\lambda 6731$ Å	6732.335	5.710 ± 0.573	6732.570	1.107 ± 0.161	6732.847	4.210 ± 0.505	6732.899	5.581 ± 0.676
$E(B - V)$ [mag]:		0.000		0.493 ± 0.040		0.403 ± 0.030		0.246 ± 0.030
SFR [$M_{\odot} \text{ yr}^{-1}$]:		0.139		0.017		0.070		0.076

Note. All fluxes are in $10^{-16} \text{ erg s}^{-1} \text{ cm}^{-2}$.

Table 5
Oxygen Abundances

Calibrator	Support Lines	Host Galaxy	SN Region $1'' \times 1''$	SN Region $3'' \times 3''$ (five spaxels)	SN Region $3'' \times 3''$ (nine spaxels)
D02 (1)	N2	$8.15 + 0.15 - 0.15$	$8.20 + 0.15 - 0.16$	$8.11 + 0.16 - 0.16$	$8.13 + 0.16 - 0.17$
PP04 N2H α (2)	N2	$8.15 + 0.02 - 0.03$	$8.17 + 0.03 - 0.04$	$8.13 + 0.03 - 0.03$	$8.14 + 0.04 - 0.04$
PP04 O3N2 (2)	N2, O3/H β	$8.10 + 0.02 - 0.02$	$8.11 + 0.04 - 0.04$	$8.07 + 0.03 - 0.04$	$8.08 + 0.04 - 0.04$
M08 N2H α (3)	N2	$8.24 + 0.05 - 0.07$	$8.30 + 0.07 - 0.08$	$8.20 + 0.07 - 0.08$	$8.22 + 0.08 - 0.09$
M13 O3N2 (4)	[N II] $\lambda 6584$ /H β , O3/H β		$8.18 + 0.01 - 0.01$	$8.18 + 0.00 - 0.00$	$8.18 + 0.01 - 0.01$
M13 N2 (4)	[N II] $\lambda 6584$ /H β	$8.13 + 0.05 - 0.05$	$8.16 + 0.06 - 0.06$	$8.11 + 0.06 - 0.06$	$8.12 + 0.06 - 0.06$
KK04 N2 α (5)	N2, q, (N2O2)	$8.26 + 0.05 - 0.07$	$8.31 + 0.08 - 0.09$	$8.21 + 0.07 - 0.08$	$8.23 + 0.09 - 0.10$
KD02comb (6)	COMBINED ^a	$8.26 + 0.05 - 0.07$	$8.31 + 0.07 - 0.09$	$8.21 + 0.07 - 0.08$	$8.23 + 0.09 - 0.10$

Note.

^a This method chooses the optimal among given: M91, KD02 N2O2, KD02 N2H α , KD04 R23, [N2, N2O2] diagnostics (Kewley & Ellison 2008).

References. (1) Denicoló et al. (2002), (2) Pettini & Pagel (2004), (3) Maiolino et al. (2008), (4) Marino et al. (2013), (5) Kobulnicky & Kewley (2004), (6) Kewley & Ellison (2008).

5.2. Host Long-slit Spectroscopy

We also obtained one long-slit spectrum of the host using LRIS/Keck. The LRIS spectrum is a light-weighted average of a $1'' \times 4''$ size region centered on the “nucleus” of the galaxy (i.e., the one with the strongest trace/continuum). Fluxes were measured using SPLIT in IRAF and errors calculated in the same way as for the integrated regions from the PMAS data. The fluxes are presented in Table 9 in the Appendix. We corrected all fluxes for Galactic extinction ($A_V = 0.0286$ mag).

We determined the intrinsic extinction using the Balmer decrement as described above and found no extinction based on this spectrum. This result is consistent with the value of the extinction based on the IFU integrated galaxy spectrum, but is not consistent with the extinction deduced from IFU data at the SN position, which indicates a large Balmer decrement in that region. We only see high extinction at the SN region as we explain in Section 5.1.1, where we speculated that it may be due to dust that is accumulated in a small area behind the SN. Hence, without clear emission lines, the extracted LRIS

Table 6
Photometry of the Host of SN 2018gep Used for the SED Fitting

Filter	λ_{mean} (Å)	mag	mag _{err}
SDSS <i>u'</i>	3600.0	19.556	0.045
SDSS <i>g'</i>	4700.0	18.852	0.012
SDSS <i>r'</i>	6200.0	18.828	0.016
SDSS <i>i'</i>	7500.0	18.788	0.020
SDSS <i>z'</i>	8900.0	18.656	0.067
GALEX NUV	2315.7	19.912	0.009
GALEX FUV	1538.6	20.074	0.020

spectrum with area of $1'' \times 4''$ centered on the galaxy “nucleus,” may miss some light from the SN region.

In the Keck spectrum we detect the same lines as in the integrated IFU spectrum, and additionally we measure the [S III] lines at $\lambda 9069$ and 9532 Å. We then also derive metallicities using the pyMCZ code as described above, and present the results in the Appendix, Table 10. The results from the Keck spectrum are consistent with the metallicities found for the same calibrators in the integrated galaxy spectrum of the PMAS data.

5.3. SED Fit

The host galaxy is a blue dwarf galaxy, with an observed SDSS mag of $g' = 18.87$ mag, and with a diameter of $\sim 10''$. We use the Le Phare code to perform SED fitting of the host galaxy of SN 2018gep using broadband data from the SDSS. The physical parameters were calculated using Bruzual & Charlot (2003) population synthesis models as galaxy templates. We use the photometry (corrected for the Galactic extinction of $A_V = 0.0286$ mag) presented in Table 6.

Our best fit has a reduced χ^2 of ~ 1 ($\chi^2 = 4.86$). In Figure 10 we show the SED fit of the host galaxy, and the physical parameters derived are listed in Table 7.

Using this SED fitting method we infer the SFR to be $\text{SFR} = 0.048_{-0.010}^{+0.054} M_{\odot} \text{ yr}^{-1}$, while the values of the SFR based on the emission-line analysis ranges from 0.017 to $0.139 M_{\odot} \text{ yr}^{-1}$, for the SN region ($1'' \times 1''$ area) and the whole galaxy, respectively. The SED reveals the total mass to be equal to $M = (7.75_{-1.22}^{+2.44}) \times 10^7 M_{\odot}$, and implies that it is a young galaxy with an age of $0.32_{-0.05}^{+0.01}$ Gyr. Our values are consistent within our 1σ errors with those of Ho et al. (2019a) (who do not report uncertainties), though lower than theirs (probably because we did not include NIR data, which they did).

5.4. Comparison with Other SN Hosts

Most star-forming galaxies follow the fundamental mass-metallicity relationship (e.g., Tremonti et al. 2004) in which higher-mass galaxies also have high metallicity. Thus comparing the host galaxy of SN 2018gep to those of other transients and to the general population of star-forming galaxies as traced by the SDSS (Kewley & Ellison 2008) may give us clues about the stellar population that preferentially produces those explosions.

In Figure 11 we compare the host mass and metallicity in the KD02 (Kewley & Dopita 2002) scale against the values for hosts of other SNe Ic-bl, GRB-SNe and Fast Evolving Transients. The hosts of SN 2018gep and iPTF16asu are low-mass, low-metallicity dwarf galaxies that lie beneath the observed SDSS population and its standard deviation

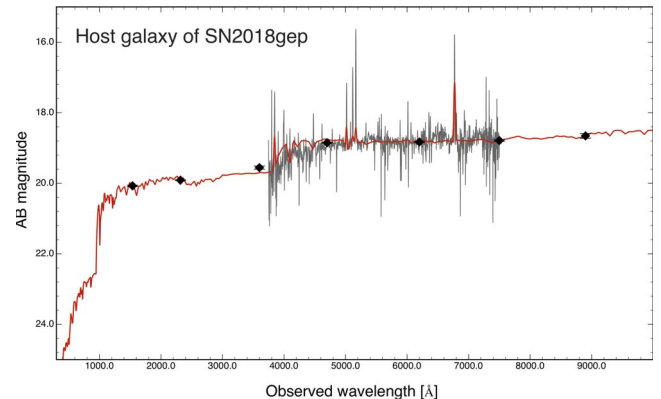


Figure 10. Spectral energy distribution fit to the photometric data of the host galaxy of SN 2018gep (red line). We plot the spectrum of the galaxy (gray) and the photometric information for different filters (black diamonds). The plot shows the wavelength range of 300 – 10^4 Å. The SN 2018gep host-galaxy spectrum plotted in the figure was corrected for Galactic extinction and calibrated using SDSS photometry ($m - m_0 = 0.26$ mag).

Table 7
Physical Parameters of the Host of SN 2018gep Derived Using SED Fitting to Source Photometry

Parameter [Unit]	Value
Age [Gyr]	$0.32_{-0.05}^{+0.01}$
$M [10^7 M_{\odot}]$	$7.75_{-1.22}^{+2.44}$
SFR [$M_{\odot} \text{ yr}^{-1}$]	$0.048_{-0.010}^{+0.054}$
SSFR [Gyr^{-1}]	$0.622_{-0.043}^{+0.244}$
$L_{\text{NUV}} [10^7 L_{\odot}]$	5.357
$L_R [10^7 L_{\odot}]$	5.498
$L_K [10^7 L_{\odot}]$	1.088

(Kewley & Ellison 2008). The host galaxies of SN 2018gep and iPTF16asu have masses and metallicities that are broadly consistent with both the SN Ic-bl sample and the GRB-SN sample (the hosts of which are also comparable to each other; Modjaz et al. 2020). The host of iPTF16asu has both a mass and metallicity close to the average of these two samples while the host of SN 2018gep is on the very low-mass end while having a metallicity similar to the average. Comparing the hosts of SN 2018gep and iPTF16asu with those of the fast-transient hosts, we show that their host properties are on the extreme end of the observed distribution of fast-transient hosts. The host galaxies of SN 2018gep and iPTF16asu have metallicities comparable to that of the lowest measured host from the PS1 Fast Evolving Transient sample and with the SN 2018gep host galaxy having a mass similar to the least massive and most metal-poor hosts from the PS1 sample simultaneously. In general the population of host galaxies of Fast Evolving Transients contains objects with masses and metallicities higher than those of SNe Ic-bl or GRB-SNe.

The host galaxies from Pursiainen et al. (2018) are not shown in Figure 11, as these galaxies had no reported metallicities. However, recent results from Wiseman et al. (2020) using the host galaxies from Pursiainen et al. (2018) have found that the host galaxy Dark Energy Survey (DES) sample of Rapidly Evolving Transients lie in a similar space as the SNe Ic-bl and GRB-SNe samples. The metallicity metrics used by Wiseman et al. (2020) are different from those used here (PP04-O3N2 versus KD02). Interestingly, their transient

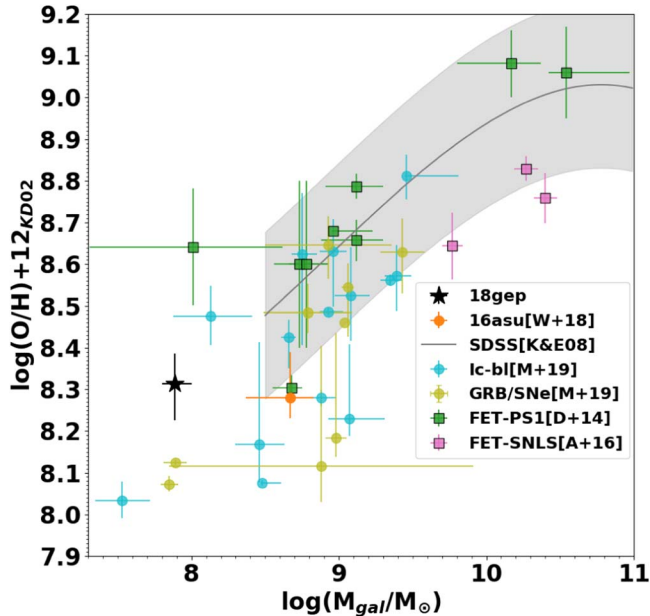


Figure 11. Mass–metallicity relation of the hosts of SN 2018gep (this work) and iPTF16asu (Whitesides et al. 2017), compared to the SDSS galaxy sample (gray region; Kewley & Ellison 2008), the iPTF Ic-bl SNe sample (Modjaz et al. 2020), PS1 Fast Evolving Transients (Drout et al. 2014) and SuperNova Legacy Survey Fast Evolving Transients (Arcavi et al. 2016). All values were converted to the KD02 (Kewley & Dopita 2002) metallicity scale using Bianco et al. (2014) and published emission-line values where available, or conversion relations from Kewley & Ellison (2008) in the remaining cases.

sample (from Pursiainen et al. 2018) does not require a strictly blue color, some of their objects are red, and for example could include objects such as PTF10vgv (see Figure 5), which lacks the strong blue colors but does evolve quite rapidly. The significant, systematic offset between the host galaxies of the PS1 sample and the DES sample likely implies either different intrinsic objects or a bias due to detection/selection method (Wiseman et al. 2020); and the host of SN 2018gep is not a clear match to either of these samples.

6. Discussion

6.1. Comparison with Standard Models

As we have discussed in Sections 3 and 4 SN 2018gep, while possessing the broad lines with high absorption velocities that are the defining characteristics of an SN Ic-bl, also appears to be an outlier in the general population of SNe Ic-bl as it exhibits an anomalous early blue rise and is on the luminous end of the SN Ic-bl absolute magnitude distribution. We conclude that not only is SN 2018gep different observationally from other observed SNe Ic-bl, but that it also requires a different (or at least additional) source of energy injection which is consistent with its location in Figure 4.

We compare the observed SN 2018gep light curve with simple semi-analytic model fits using the MOSFiT package (Guillochon et al. 2018) in Figure 12. For the MOSFiT Ic SN model, we see that this standard model (Ni-powered explosive SNe; Pankey 1962; Arnett 1982; Nadyozhin 1994) has a difficult time reproducing the rapid blue rise seen in the observed data. If we add an additional source of energy injection, here magnetar spin-down (Kasen & Bildsten 2010; Woosley 2010; Nicholl et al. 2017) or

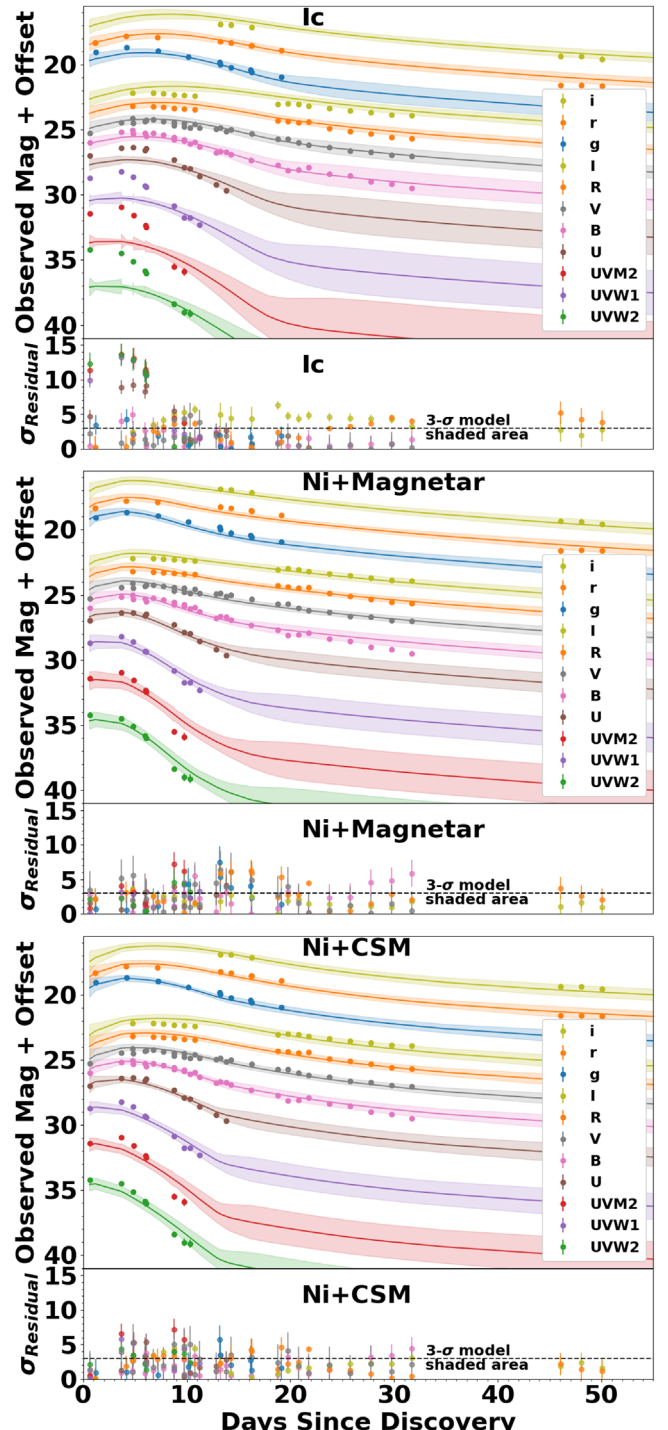


Figure 12. Simple semi-analytic model fits to the observed SN 2018gep data using the MOSFiT (Guillochon et al. 2018) package and NiCo decay ‘Ic’ (Nadyozhin 1994), magnetar+NiCo decay (Nicholl et al. 2017), and CSM-interaction+NiCo decay (Chatzopoulos et al. 2013) models. The median (solid) and 3σ (shaded) region of the final best-fit distribution of model data are shown with the residuals plot corresponding to the magnitude residual of the observed data scaled by the standard deviation of the models at that epoch; e.g., $(m_{\text{obs}}(t) - m_{\text{model}}(t, \theta)) / \sigma_{\text{model}}(t, \theta)$ with the region below the dotted line in residuals corresponding to the shaded region of the light curves. The pure Ni+Co decay model has difficulty reproducing the observed rapid, blue rise with residuals comparable to those shown in the comparison with the observed population shown in Figure 5 (as expected of a Type Ic SNe model), while the addition of an additional power source significantly improves the fit.

Table 8

Best-fit Model Parameters in the MOSFIT Package for Powering the UV–Optical Light Curves of SN 2018gep (Figure 12)

Parameter [Unit]	Ic	Ni+Mag	Ni+CSM
$\log M_{\text{ej}} [M_{\odot}]$	$-0.12^{+0.03}_{-0.04}$	$-0.58^{+0.08}_{-0.06}$	$-0.31^{+0.19}_{-0.19}$
$\log f_{\text{Ni}}$	$-0.01^{+0.002}_{-0.01}$	$-0.30^{+0.17}_{-0.17}$	$-0.56^{+0.32}_{-0.25}$
$t_{\text{exp}} [\text{days}]$	$-5.42^{+0.64}_{-0.74}$	$-2.4^{+0.53}_{-0.75}$	$-1.9^{+0.50}_{-0.67}$
$\log v_{\text{ej}} [\text{km s}^{-1}]$	$4.50^{+0.04}_{-0.06}$	$4.45^{+0.4}_{-0.70}$	$4.7^{+0.21}_{-0.27}$
$\log \kappa [\text{cm}^2 \text{ g}^{-1}]$	$-0.98^{+0.03}_{-0.02}$	$-0.15^{+0.23}_{-0.18}$	$-0.24^{+0.33}_{-0.33}$
$\log n_{\text{H,host}}$	$17.66^{+0.93}_{-1.13}$	$20.49^{+0.53}_{-1.92}$	$17.94^{+1.52}_{-1.40}$
$\log \sigma$	$-0.08^{+0.03}_{-0.02}$	$-0.26^{+0.03}_{-0.03}$	$-0.27^{+0.03}_{-0.02}$
$\log T_{\text{min}} (\text{K})$	$3.63^{+0.03}_{-0.03}$		$3.75^{+0.02}_{-0.02}$
$\log B$		$0.97^{+0.02}_{-0.04}$	
$M_{\text{NS}} (M_{\odot})$		$1.04^{+0.07}_{-0.03}$	
$P_{\text{spin}} (\text{ms})$		$8.16^{+1.43}_{-3.02}$	
$\theta_{\text{PB}} (\text{rad})$		$1.34^{+0.15}_{-0.17}$	
$\log M_{\text{CSM}}$			$-0.97^{+0.04}_{-0.02}$
$\log \rho$			$-11.27^{+0.06}_{-0.06}$

Note. Best-fit values and 2σ errors for model parameters. See Guillochon et al. (2018), Chatzopoulos et al. (2013), Nicholl et al. (2017), and Nadyozhin (1994) for parameter details. We caution that models like these are generally best used for population studies of objects that are well fit by standard models, and want to emphasize that the work here is most illustrative of how this is not a “typical” SNe Ic-bl and that the inclusion of additional physics is necessary.

CSM interaction (Chatzopoulos et al. 2013), we see that the early fit improves significantly. This is overall consistent with our previous conclusion that SN 2018gep is both different from a typical SN Ic-bl and most likely has an additional, or different, source of energy injection. We caution that models like these are generally best used for population studies of objects that are well fit by standard models, and want to emphasize that the work here is most illustrative of how this is not a “typical” SNe Ic-bl and that the inclusion of additional physics is necessary.

The best-fit model parameters for the three discussed models can be seen in Table 8. As these are simple semi-analytic models, the physical inference possible in such a unique case is somewhat limited. Overall, the standard Ic model requires a significant overabundance of Ni but most closely matches the ejecta velocity and explosion date inferred from the obtained data. The Ni+ energy injection models tend to have a more realistic Ni fraction while undershooting the ejecta velocity and being on the edge of allowed explosion dates.

Of the two models with some additional non- ^{56}Ni energy injection, the magnetar model requires a large magnetic field, $B \sim 10^{14}$ G, which is comparable to that required for SLSNe by similar models (Nicholl et al. 2017).

Could SN 2018gep be a transitional object between “ordinary” SNe Ic-bl and SLSNe Ic, given its high luminosity and blue colors which are similar to those of SLSNe? There are certainly some similarities, but also some significant differences. SN 2018gep does show some similarities to those of SLSNe in the spectral features, with the detection of the “W” feature in the spectra at early times (Ho et al. 2019a). On the other hand, the spectra of SN 2018gep are much bluer than those of SLSNe Ic at both phases that we cover. Photometrically, the peak luminosity of SN 2018gep is comparable to that of some SLSNe and does lie between that of the SN Ic-bl sample and the SLSN sample. However, the light curve shape of SN 2018gep evolves much faster, with rise times significantly shorter than both SNe Ic-bl and SLSNe (i.e., SN 2018gep does not lie between the locus of the SN

Ic-bl and SLSN Ic samples), and does not conform to proposed light curve scaling relations for even the fastest SLSNe Ic.

While there is significant flexibility in these models, the large required value of the magnetic field most likely disfavours this energy injection method without a compelling argument for a similar compact object arising from the stellar progenitor. This would make the $^{56}\text{Ni}+\text{CSM}$ interaction model the most favored of the three models, which is consistent with the results from Ho et al. (2019a). This picture is also qualitatively similar to the theoretical explosion models of Aguilera-Dena et al. (2018) which suggest a population SNe Ic originating from high-mass progenitors that may interact with a C/O-rich CSM, although these models would similarly predict an associated long-duration GRB which is disfavored in this case (Ho et al. 2019a).

6.2. Pre-explosion Variability, CSM Interaction, and Comparison with Other Work

The work done by Ho et al. (2019a) on SN 2018gep shows the detection of pre-explosion variability and inferred mass loss by the progenitor star and the subsequent interaction between the pre-explosion ejected mass and the SN shock. This is a well-substantiated and physically motivated model for SN 2018gep that is overall consistent with our more general and data-driven discovery that some additional source of energy injection needs to be present early on in the light curve.

The similarity between SN 2018gep and the PS1 and DES Fast Evolving Transients, while also noted by Ho et al. (2019a), is not studied in significant detail by them as we do here, including our light curve and environment studies and folding iPTF16asu into this as well. We find some similarity to both SLSNe (though SN 2018gep has an even bluer spectrum pre-max than SLSNe) and GRB-SNe (in the light curve and spectra) which is consistent with the Ho et al. (2019a) findings of potential SLSNe spectral features and the high velocities only seen otherwise in GRB-SNe.

7. Conclusion—Fast Blue Optical Transients, SN Ic-bl, or Both?

SN 2018gep is an SN Ic-bl with anomalously blue colors ($\gtrsim 4$ mag in $uvw2 - v$ or ~ 2 mag in $g-r$) at early epochs and a rapid rise time ($t_{\text{rise}} = 5.6 \pm 0.5$ days). This anomalous behavior is also seen in its early blue, nearly featureless spectrum, which at later times (after maximum light) shows more significant absorption lines while maintaining its atypical blue continuum. With a host metallicity of $\log(\text{O/H})+12 = 8.31^{+0.07}_{-0.09}$ (from the SN region) and host galaxy mass of $M_{\text{host}} = 7.8^{+2.4}_{-1.2} \times 10^7 M_{\odot}$, it is within the typically observed range of SN Ic-bl host parameters and on the edge of the FBOT host-property distribution. All these properties place SN 2018gep as a significant outlier when compared with other SNe Ic-bl except for iPTF16asu, while at the same time it is on the edge of the observed parameter space for FBOTs. In addition to these derived properties, its general photometric evolution occurs in a highly similar manner to the observed PS1 FBOTs (PanSTARRS; Drout et al. 2014), which is the only FBOT sample with well-observed rise times. When compared with simple analytical SN Ic models, we see that the standard SN Ic model has difficulty reproducing the rapid blue rise while the post-peak data are more well-matched by the models. We find that an additional energy-injection mechanism

(here, CSM interaction or magnetar coupling) improves the early-time fit significantly.

The observations of SN 2018gep highlight the time-dependent (and to a lesser extent sensitivity-dependent) nature of our classification schemes for these mysterious transients. If we had poorer-quality observations of iPTF16asu and SN 2018gep we would have likely just called these events FBOTS given their blue colors, rapid rises, and nearly featureless blue spectra before and around maximum light. However, if we had only obtained late observations (or had fewer colors) we would have likely classified SN 2018gep as a more standard SN Ic-bl given that its later spectra and colors are more closely matched to the broader SN Ic-bl sample and that the later light curve is well-fit by the typical models. In fact, if only red data (i.e., rest-frame g' -band filter and redward) had been obtained, as is common in many transient surveys, this SN would have looked much more similar to the SN Ic-bl sample as a whole and the generic analytical ^{56}Ni -driven model would have produced a reasonable fit to the data. Similarly, if the early emission had been missed (e.g., $t < 10$ days after discovery), this object would have appeared more like a typical SN Ic-bl. This object highlights the need for missions such as Swift (Gehrels et al. 2004) and the proposed Gravitational-wave Ultraviolet Counterpart Imager (GUCI) Network (Cenko 2019), which enable the prompt UV observations crucial for classification as well as our understanding of the atypical explosion and energy-injection mechanisms of transient events like this.

However, with a fortuitous object that is bright, nearby, and discovered promptly—such as SN 2018gep—it is possible to acquire a detailed data set including early-time data with high cadence and colors, multi-wavelength information, a spectral time series, and host galaxy observations, all of which we present here. It is only this more complete data set that illustrates the SN transitioning from a rapidly rising blue transient to an SN Ic-bl, and this photometric and spectroscopic evolution may provide some insight into other observed FBOTS and extreme SNe Ic-bl.

When compared against the PS1-FBOT sample (the only such with host information and measured rise times), both SN 2018gep and iPTF16asu show a similar photometric rise and decline time. While the color data are noisy, due to the simplistic comparison across redshifts performed with minimum assumptions in addition to the intrinsic variability of the observed FBOT sample, the observed results for both of these objects lie well within the observed PS1-FBOT distribution. The host environments of SN 2018gep and iPTF16asu occupy a similar region of the host-galaxy mass versus metallicity distribution as the other SN Ic-bl and GRB-SNe from Modjaz et al. (2020) and are on the edge of the observed Fast Evolving Transient host phase space.

Not all of the observed FBOTS (or even all FBOTS in the PS1 sample only) can be like SN 2018gep or iPTF16asu. The observed FBOTS span too broad a range of host environments and intrinsic magnitudes to be consistent with the general SN Ic-bl and GRB-SNe sample. Furthermore, while many FBOTS have similar photometric evolution, there are notable exceptions, such as AT 2018cow (Prentice et al. 2018; Perley et al. 2019) with its rapid evolution but minimal color evolution and one object in the PS1 sample with emission on longer timescales. While we do not have radio or X-ray data from the Drout et al. (2014) sample, another major difference between SN 2018gep and AT 2018cow is the radio and X-ray emission which was detected in AT

2018cow (Ho et al. 2019b; Margutti et al. 2019) while it was not in SN 2018gep (Ho et al. 2019a). Furthermore, Arcavi et al. (2016) compare a number of power sources and conclude that from their samples not all similar events can be powered by the same source. There is a need for significantly more multi-epoch spectra across FBOTS as a whole, as we cannot make strong conclusions without a greater sample of significantly pre- and post-peak spectra.

However, we speculate that if the physical explosion of SN 2018gep and iPTF16asu is that of an SN Ic-bl with a rapid blue rise driven by an additional source of energy injection, then perhaps the FBOTS with similar photometric evolution (e.g., most of the PS1 sample and many others) could share a similar explosion or energy-injection mechanism. It could be that this energy-injection mechanism drives the observed early blue rise common to the sample, but with differing progenitor stars (and underlying SNe) that may lead to much of the observed variance in the sample.

This model—a variety of underlying explosions with an additional source of early blue emission—would be consistent with the reports of pre-explosion variability and a CSM-interaction-driven model by Ho et al. (2019a), and perhaps one diagnostic of this common FBOT energy-injection mechanism might be a systematic search for pre-explosion variability across a larger sample of well-studied FBOT SNe. While historically difficult to do, the increasing cadence and depth of large-area synoptic surveys is making this increasingly feasible. In the future, the Vera Rubin Observatory Legacy Survey of Space and Time will be able to fortuitously provide pre-explosion images throughout the survey’s 10 year duration, enabling the search for signatures of a common energy-injection mechanism. Another key to further understanding the nature of these events will be the acquisition of multi-epoch spectroscopy for a significant sample size of Fast Evolving Transients. Time-series spectra allow us to test our hypothesis whether, as a sample, these objects develop significant variations at later times from their featureless blue continuum around maximum light, and if they evolve similarly or with significant diversity. Additional UV observations (whether from Swift, GUCI, or another mission) will similarly be key as the modestly blue optical colors as seen in SN 2018gep belied a significantly greater UV flux, and understanding how common and energetic this blue emission is will allow us to further constrain the explosion mechanism and progenitor.

This research made use of Astropy,²² a community-developed core Python package for Astronomy (Astropy Collaboration et al. 2013; Price-Whelan et al. 2018).

Some of the data presented herein were obtained at the W. M. Keck Observatory, which is operated as a scientific partnership among the California Institute of Technology, the University of California and the National Aeronautics and Space Administration. The Observatory was made possible by the generous financial support of the W. M. Keck Foundation. The authors wish to recognize and acknowledge the very significant cultural role and reverence that the summit of Maunakea has always had within the indigenous Hawaiian community. We are most fortunate to have the opportunity to conduct observations from this mountain.

²² <http://www.astropy.org>

T.P. acknowledges support from NASA under the Swift GI grant 1619152, the Tess GI grant G03267, from the NYU Center for Cosmology and Particle Physics, from a 19 Washington Square North Award awarded to M.M, and in part by a grant from the New York University Research Challenge FundProgram.

M.M. and the SNYU group have been supported by the NSF CAREER award AST-1352405, by the NSF award AST-1413260, and by a Humboldt Faculty Fellowship. M.M. is grateful for her sabbatical stay supported by the Center for Computational Astrophysics at the Flatiron institute and for the hospitality of the Max-Planck Institute for Astronomy, Heidelberg, during which some of this work was accomplished.

K.B. acknowledges financial support from the Ministerio de Economía y Competitividad through the Spanish grant BES-2014-069767. K.B., C.T. and A.d.U.P. acknowledge support from the Spanish research project AYA2017-89384-P. C.T. acknowledges support from funding associated to a Ramón y Cajal fellowship RyC-2012-09984. A.d.U.P. acknowledges support from funding associated to a Ramón y Cajal fellowship RyC-2012-09975. L.I. acknowledges support from funding associated to a Juan de la Cierva Incorporación fellowship IJCI-2016-30940. D.A.K. acknowledges support from the Spanish research projects AYA 2014-58381-P, AYA2017-89384-P, from Juan de la Cierva Incorporación fellowship IJCI-2015-26153, and from Spanish National Project research project RTI2018-098104-J-I00 (GRBPhot).

J.V. and his research group at Konkoly Observatory is supported by the “Transient Astrophysical Objects” GINOP 2.3.2-15-2016-00033 project of the National Research, Development and Innovation Office (NKFIH), Hungary, funded by the European Union. K.V. and L.K. thank the financial support from the National Research, Development and Innovation Office (NKFIH), Hungary, under grants NKFI-K-131508 and NKFI-KH-130526. A.B. and K.V. are supported by the Lendület program grant LP2018-7/2019 of the Hungarian Academy of Sciences. T.N.D. also acknowledges the support of the Hungarian OTKA grant No. 119993.

The work of X.W. was funded by the National Science Foundation of China (NSFC grants 12033003, 11633002, and 11761141001), the Major State Basic Research Development Program (grant No. 2016YFA0400803), and the Scholar Program of Beijing Academy of Science and Technology (DZ:BS202002).

L.G. was funded by the European Union’s Horizon 2020 research and innovation program under the Marie Skłodowska-Curie grant agreement No. 839090. This work has been partially supported by the Spanish grant PGC2018-095317-B-C21 within the European Funds for Regional Development (FEDER).

R.G.B. acknowledges financial support from the Spanish Ministry of Economy and Competitiveness through grant AYA2016-77846-P and from the State Agency for Research of the Spanish MCIU through the “Center of Excellence Severo Ochoa” award to the Instituto de Astrofísica de Andalucía (SEV-2017-0709).

These observations made use of the LCO network. D.A.H., C.P., D.H., and J.B. are supported by NSF Grant AST-1911225 and NASA Grant 80NSSC19k1639.

Facilities: Keck:I (LRIS), Sloan, Konkoly:Schmidt.

Software: astropy (Astropy Collaboration et al. 2013; Price-Whelan et al. 2018), MOSFiT (Guillochon et al. 2018), SNID (Blondin & Tonry 2007), pyMCZ (Bianco et al. 2016), Le Phare (Arnouts et al. 1999; Ilbert et al. 2006).

Appendix

Host Galaxy Analysis Details: IFU and Long-slit Spectra

We give supplementary information to the data reduction and analysis described in Section 4. In Figure 13 we present host-galaxy maps of commonly used emission lines. In Figure 14 we present maps of the derived host-galaxy metallicities for a selection of calibrators. In Table 9 we present emission-line fluxes from the long-slit LRIS spectrum obtained from the W.M. Keck Telescope. In Table 10 we present the derived metallicities using the emission lines from the Keck spectrum for a variety of calibrators. In general we find reasonable agreement between the properties derived from the Keck spectrum and spatially averaged properties of the IFU data.

Table 9
Emission-line Fluxes from the LRIS Long-slit Spectrum with Galactic-extinction Correction Applied

Emission Line	λ (Å)	Host Galaxy
[O II] λ 3727 Å	3726.5000	35.57 ± 0.7475
H β λ 4861 Å	4859.3460	21.13 ± 0.3292
[O III] λ 4959 Å	4956.8080	35.10 ± 0.3747
[O III] λ 5007 Å	5004.7220	104.0 ± 0.6245
[O I] λ 6300 Å	6298.3150	0.668 ± 0.0603
H α λ 6563 Å	6561.6660	56.62 ± 0.3015
[N II] λ 6584 Å	6582.9170	1.547 ± 0.05567
[S II] λ 6717 Å	6715.4190	3.384 ± 0.08153
[S II] λ 6731 Å	6729.7800	2.506 ± 0.07482
[S III] λ 9069 Å	9068.5210	2.503 ± 0.04833
[S III] λ 9532 Å	9530.5660	7.763 ± 0.1247

Note. All fluxes are in 10^{-16} erg s $^{-1}$ cm $^{-2}$.

Table 10
Derived Oxygen Abundance Based on the LRIS Long-slit Spectrum in Different Scales Using the Code from Bianco et al. (2016)

Calibrator	Host Galaxy
D02	$7.979 + 0.157 - 0.166$
Z94	$8.440 + 0.004 - 0.003$
M91	$8.077 + 0.015 - 0.015$
PP04 N2Ha	$8.053 + 0.007 - 0.007$
PP04 O3N2	$8.008 + 0.006 - 0.005$
P10 ONS	$8.933 + 0.025 - 0.025$
P10 ON	$7.888 + 0.035 - 0.035$
M08 N2Ha	$8.033 + 0.015 - 0.015$
M08 O3O2	$8.059 + 0.009 - 0.010$
M13 N2	$8.018 + 0.046 - 0.045$
KD02 N2O2	$7.601 + 0.035 - 0.031$
KK04 N2Ha	$8.250 + 0.015 - 0.016$
KK04 R23	$8.286 + 0.012 - 0.013$
KD02comb	$8.182 + 0.014 - 0.014$

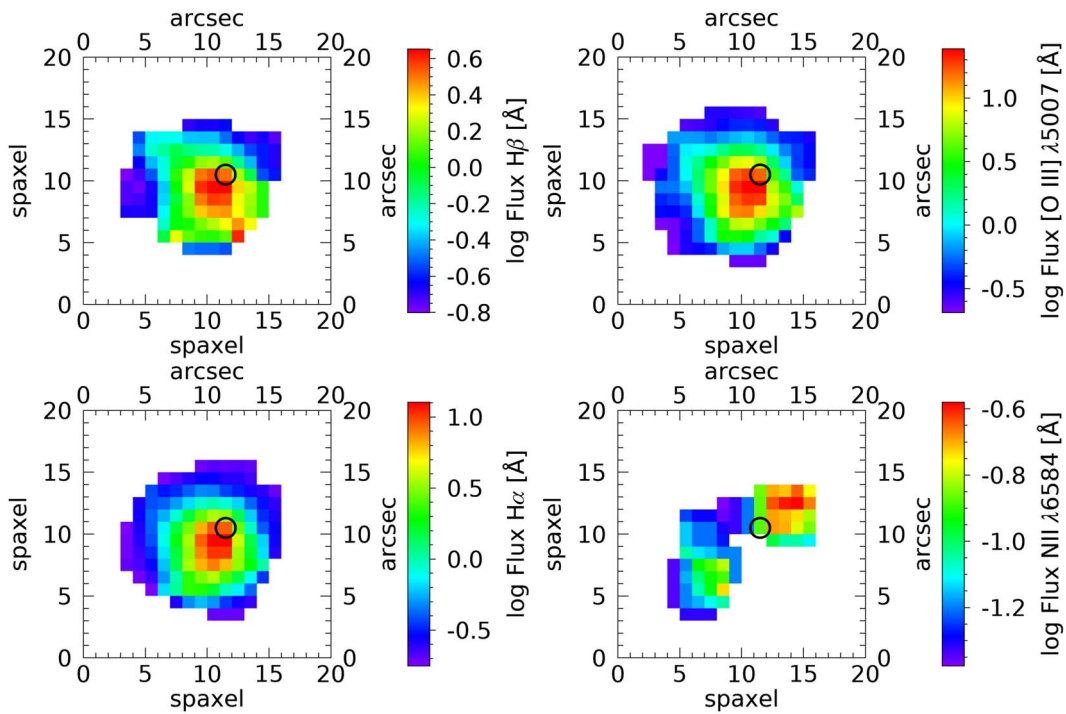


Figure 13. Distribution map of the emission-line fluxes in the SN 2018gep host galaxy: H β , [O III] λ 5007 \AA , H α , [N II] λ 6584 \AA . The black circle indicates the position of SN 2018gep.

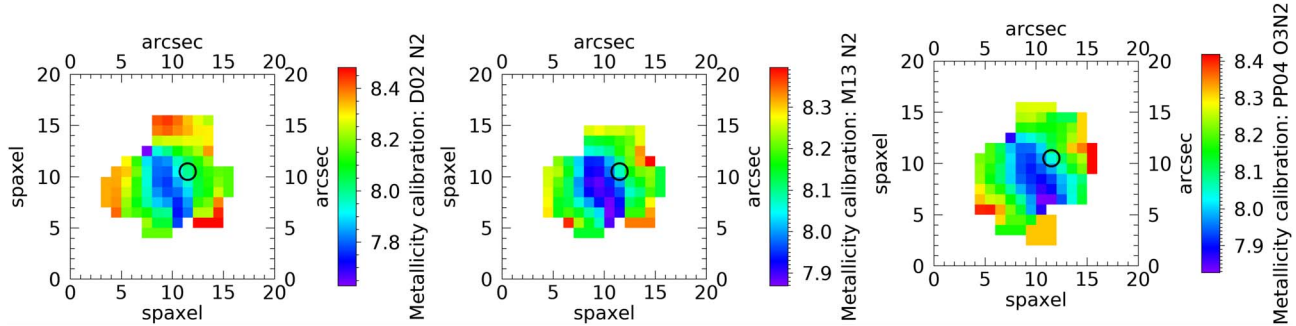


Figure 14. Maps of the SN 2018gep host-galaxy metallicities derived with different metallicity calibrations, using the N2 parameter from the Kewley & Dopita (2002) calibration (left), N2 parameter in the Marino et al. (2013) calibration (middle), and O3N2 parameter in the calibration of Pettini & Pagel (2004) (right). The black circle indicates the position of SN 2018gep.

ORCID iDs

T. A. Pritchard <https://orcid.org/0000-0001-9227-8349>
 Maryam Modjaz <https://orcid.org/0000-0001-7132-0333>
 Marc Williamson <https://orcid.org/0000-0003-2544-4516>
 Christina C. Thöne <https://orcid.org/0000-0002-7978-7648>
 J. Vinkó <https://orcid.org/0000-0001-8764-7832>
 Federica B. Bianco <https://orcid.org/0000-0003-1953-8727>
 Jamison Burke <https://orcid.org/0000-0003-0035-6659>
 Rubén García-Benito <https://orcid.org/0000-0002-7077-308X>
 L. Galbany <https://orcid.org/0000-0002-1296-6887>
 Daichi Hiramatsu <https://orcid.org/0000-0002-1125-9187>
 D. Andrew Howell <https://orcid.org/0000-0003-4253-656X>
 Luca Izzo <https://orcid.org/0000-0001-9695-8472>
 D. Alexander Kann <https://orcid.org/0000-0003-2902-3583>
 Curtis McCully <https://orcid.org/0000-0001-5807-7893>
 Craig Pellegrino <https://orcid.org/0000-0002-7472-1279>
 Stefano Valenti <https://orcid.org/0000-0001-8818-0795>
 Xiaofeng Wang <https://orcid.org/0000-0002-7334-2357>

J. C. Wheeler <https://orcid.org/0000-0003-1349-6538>
 Danfeng Xiang <https://orcid.org/0000-0002-1089-1519>
 K. Sárnczky <https://orcid.org/0000-0003-0926-3950>
 A. Bódi <https://orcid.org/0000-0002-8585-4544>
 D. Tarczay-Néhéz <https://orcid.org/0000-0003-3759-7616>
 A. Pál <https://orcid.org/0000-0001-5449-2467>
 R. Szakáts <https://orcid.org/0000-0002-1698-605X>
 K. Vida <https://orcid.org/0000-0002-6471-8607>

References

Aguado, D. S., Ahumada, R., Almeida, A., et al. 2019, *ApJS*, 240, 23
 Aguilera-Dena, D. R., Langer, N., Moriya, T. J., & Schootemeijer, A. 2018, *ApJ*, 858, 115
 Anderson, J. P., James, P. A., Habergham, S. M., Galbany, L., & Kuncarayakti, H. 2015, *PASA*, 32, e019
 Arcavi, I., Wolf, W. M., Howell, D. A., et al. 2016, *ApJ*, 819, 35
 Arnett, W. D. 1982, *ApJ*, 253, 785
 Arnouts, S., Cristiani, S., Moscardini, L., et al. 1999, *MNRAS*, 310, 540
 Astropy Collaboration, Robitaille, T. P., Tollerud, E. J., et al. 2013, *A&A*, 558, A33

Barnes, J., Duffell, P. C., Liu, Y., et al. 2018, *ApJ*, **860**, 38

Bellm, E. C., Kulkarni, S. R., Graham, M. J., et al. 2019, *PASP*, **131**, 018002

Bianco, F. B., Modjaz, M., Hicken, M., et al. 2014, *ApJS*, **213**, 19

Bianco, F. B., Modjaz, M., Oh, S. M., et al. 2016, *A&C*, **16**, 54

Blondin, S., & Tonry, J. L. 2007, *ApJ*, **666**, 1024

Bruzual, G., & Charlot, S. 2003, *MNRAS*, **344**, 1000

Burke, J., Arcavi, I., Hiramatsu, D., et al. 2018, Transient Name Server Classification Report, **2018-1442**, IAU Supernova Working Group

Calzetti, D., Armus, L., Bohlin, R. C., et al. 2000, *ApJ*, **533**, 682

Campana, S., Mangano, V., Blustin, A. J., et al. 2006, *Natur*, **442**, 1008

Cano, Z. 2013, *MNRAS*, **434**, 1098

Cano, Z., Wang, S.-Q., Dai, Z.-G., & Wu, X.-F. 2017, *AdAst*, **2017**, 1

Cano, Z., Wang, S.-Q., Dai, Z.-G., & Wu, X.-F. 2017, *AdAst*, **2017**, 8929054

Cenko, S. B. 2019, AAS Meeting Abstracts, **234**, 212.03

Chambers, K. C., Magnier, E. A., Metcalfe, N., et al. 2016, arXiv:1612.05560

Chatzopoulos, E., Wheeler, J. C., Vinko, J., Horvath, Z. L., & Nagy, A. 2013, *ApJ*, **773**, 76

Corsi, A., Gal-Yam, A., Kulkarni, S. R., et al. 2016, *ApJ*, **830**, 42

Corsi, A., Ofek, E. O., Gal-Yam, A., et al. 2012, *ApJL*, **747**, L5

De Cia, A., Gal-Yam, A., Rubin, A., et al. 2018, *ApJ*, **860**, 100

Denicoló, G., Terlevich, R., & Terlevich, E. 2002, *MNRAS*, **330**, 69

Domínguez, A., Siana, B., Henry, A. L., et al. 2013, *ApJ*, **763**, 145

Drout, M. R., Chornock, R., Soderberg, A. M., et al. 2014, *ApJ*, **794**, 23

Filippenko, A. V. 1997, *ARA&A*, **35**, 309

Gal-Yam, A. 2017, Observational and Physical Classification of Supernovae (Berlin: Springer International), 195

Gal-Yam, A. 2019, *ARA&A*, **57**, 305

Galbany, L., Anderson, J. P., Sánchez, S. F., et al. 2018, *ApJ*, **855**, 107

Galbany, L., Stanishev, V., Mourão, A. M., et al. 2014, *A&A*, **572**, A38

Galbany, L., Stanishev, V., Mourão, A. M., et al. 2016, *A&A*, **591**, A48

García-Benito, R., Díaz, A., Hägele, G. F., et al. 2010, *MNRAS*, **408**, 2234

García-Benito, R., Zibetti, S., Sánchez, S. F., et al. 2015, *A&A*, **576**, A135

Gehrels, N., Chincarini, G., Giommi, P., et al. 2004, *ApJ*, **611**, 1005

Green, G. M., Schlafly, E., Zucker, C., Speagle, J. S., & Finkbeiner, D. 2019, *ApJ*, **887**, 93

Guevel, Z., & Hosseinzadeh, G. 2017, dguevel/PyZOGY: Initial Release, v0.0.1, Zenodo, doi:10.5281/zenodo.1043973

Guillochon, J., Nicholl, M., Villar, V. A., et al. 2018, *ApJS*, **236**, 6

Henden, A. A., Welch, D. L., Terrell, D., & Levine, S. E. 2009, AAS Meeting Abstracts, **214**, 407.02

Ho, A., Schulze, S., Perley, D., et al. 2018, Transient Name Server Discovery Report, **2018-1357**, IAU Supernova Working Group

Ho, A. Y. Q., Goldstein, D. A., Schulze, S., et al. 2019a, *ApJ*, **887**, 169

Ho, A. Y. Q., Kulkarni, S. R., Perley, D. A., et al. 2020, *ApJ*, **902**, 86

Ho, A. Y. Q., Phinney, E. S., Ravi, V., et al. 2019b, *ApJ*, **871**, 73

Husemann, B., Jahnke, K., Sánchez, S. F., et al. 2013, *A&A*, **549**, A87

Ilbert, O., Arnouts, S., McCracken, H. J., et al. 2006, *A&A*, **457**, 841

Inserra, C. 2019, *NatAs*, **3**, 697

Irwin, C. M., & Chevalier, R. A. 2016, *MNRAS*, **460**, 1680

Izzo, L., Auchettl, K., Hjorth, J., et al. 2020, *A&A*, **639**, L11

Kann, D. A., Schady, P., Olivares, E., et al. 2019, *A&A*, **624**, A143

Kasen, D., & Bildsten, L. 2010, *ApJ*, **717**, 245

Kasliwal, M. M., Kulkarni, S. R., Gal-Yam, A., et al. 2012, *ApJ*, **755**, 161

Kelz, A., Verheijen, M. A. W., Roth, M. M., et al. 2006, *PASP*, **118**, 129

Kennicutt, R. C., Tamblyn, J., Congdon, C. E., et al. 1994, *ApJ*, **435**, 22

Kewley, L. J., & Dopita, M. A. 2002, *ApJS*, **142**, 35

Kewley, L. J., & Ellison, S. L. 2008, *ApJ*, **681**, 1183

Kobulnicky, H. A., & Kewley, L. J. 2004, *ApJ*, **617**, 240

Kuncarayakti, H., Anderson, J. P., Galbany, L., et al. 2018, *A&A*, **613**, A35

Kuncarayakti, H., Doi, M., Aldering, G., et al. 2013a, *AJ*, **146**, 30

Kuncarayakti, H., Doi, M., Aldering, G., et al. 2013b, *AJ*, **146**, 31

Liu, Y.-Q., Modjaz, M., & Bianco, F. B. 2017, *ApJ*, **845**, 85

Liu, Y.-Q., Modjaz, M., Bianco, F. B., & Graur, O. 2016, *ApJ*, **827**, 90

Lunnan, R., Chornock, R., Berger, E., et al. 2018, *ApJ*, **852**, 81

Maiolino, R., Nagao, T., Grazian, A., et al. 2008, *A&A*, **488**, 463

Margutti, R., Metzger, B. D., Chornock, R., et al. 2019, *ApJ*, **872**, 18

Marino, R. A., Rosales-Ortega, F. F., Sánchez, S. F., et al. 2013, *A&A*, **559**, A114

Mazzali, P. A., Deng, J., Hamuy, M., & Nomoto, K. 2009, *ApJ*, **703**, 1624

Mazzali, P. A., Sullivan, M., Pian, E., Greiner, J., & Kann, D. A. 2016, *MNRAS*, **458**, 3455

McCarthy, J. K., Cohen, J. G., Butcher, B., et al. 1998, *Proc. SPIE*, **3355**, 81

Modjaz, M. 2011, *AN*, **332**, 434

Modjaz, M., Bianco, F. B., Siwek, M., et al. 2020, *ApJ*, **892**, 153

Modjaz, M., Blondin, S., Kirshner, R. P., et al. 2014, *AJ*, **147**, 99

Modjaz, M., Gutiérrez, C. P., & Arcavi, I. 2019, *NatAs*, **3**, 717

Modjaz, M., Kewley, L., Kirshner, R. P., et al. 2008, *AJ*, **135**, 1136

Modjaz, M., Li, W., Butler, N., et al. 2009, *ApJ*, **702**, 226

Modjaz, M., Liu, Y. Q., Bianco, F. B., & Graur, O. 2016, *ApJ*, **832**, 108

Modjaz, M., Stanek, K. Z., Garnavich, P. M., et al. 2006, *ApJL*, **645**, L21

Nadyozhin, D. K. 1994, *ApJS*, **92**, 527

Nicholl, M., Guillochon, J., & Berger, E. 2017, *ApJ*, **850**, 55

Nicholl, M., Smartt, S. J., Jerkstrand, A., et al. 2015, *MNRAS*, **452**, 3869

Oke, J. B., Cohen, J. G., Carr, M., et al. 1995, *PASP*, **107**, 375

Osterbrock, D. E., & Ferland, G. J. 2006, Astrophysics of Gaseous Nebulae and Active Galactic Nuclei (Sausalito, CA: University Science Books)

Pankey, J. T. 1962, PhD thesis, Howard University

Pérez-Montero, E., & Díaz, A. I. 2003, *MNRAS*, **346**, 105

Perley, D. A. 2019, *PASP*, **131**, 084503

Perley, D. A., Mazzali, P. A., Yan, L., et al. 2019, *MNRAS*, **484**, 1031

Pettini, M., & Pagel, B. E. J. 2004, *MNRAS*, **348**, L59

Poole, T. S., Breeveld, A. A., Page, M. J., et al. 2008, *MNRAS*, **383**, 627

Prentice, S. J., Maguire, K., Smartt, S. J., et al. 2018, *ApJL*, **865**, L3

Prentice, S. J., Mazzali, P. A., Pian, E., et al. 2016, *MNRAS*, **458**, 2973

Price-Whelan, A. M., Sipőcz, B. M., Günther, H. M., et al. 2018, *AJ*, **156**, 123

Pritchard, T. A., Roming, P. W. A., Brown, P. J., Bayless, A. J., & Frey, L. H. 2014, *ApJ*, **787**, 157

Pursiainen, M., Childress, M., Smith, M., et al. 2018, *MNRAS*, **481**, 894

Quimby, R. M., De Cia, A., Gal-Yam, A., et al. 2018, *ApJ*, **855**, 2

Quimby, R. M., Kulkarni, S. R., Kasliwal, M. M., et al. 2011, *Natur*, **474**, 487

Rest, A., Garnavich, P. M., Khatami, D., et al. 2018, *NatAs*, **2**, 307

Riess, A. G., Casertano, S., Yuan, W., Macri, L. M., & Scolnic, D. 2019, *ApJ*, **876**, 85

Rockosi, C., Stover, R., Kibrick, R., et al. 2010, *Proc. SPIE*, **7735**, 77350R

Roming, P. W. A., Kennedy, T. E., Mason, K. O., et al. 2005, *SSRv*, **120**, 95

Roth, M. M., Kelz, A., Fechner, T., et al. 2005, *PASP*, **117**, 620

Schulze, S., Ho, A. Y. Q., & Mill, A. A. 2018, *ATel*, **12032**, 1

Shappee, B., Prieto, J., Stanek, K. Z., et al. 2014, AAS Meeting Abstracts, **223**, 236.03

Shivvers, I., Filippenko, A. V., Silverman, J. M., et al. 2019, *MNRAS*, **482**, 1545

Shivvers, I., Modjaz, M., Zheng, W., et al. 2017, *PASP*, **129**, 054201

Soderberg, A. M., Kulkarni, S. R., Nakar, E., et al. 2006, *Natur*, **442**, 1014

Stritzinger, M., & Leibundgut, B. 2005, *A&A*, **431**, 423

Taddia, F., Sollerman, J., Fremling, C., et al. 2019, *A&A*, **621**, A71

Taddia, F., Sollerman, J., Leloudas, G., et al. 2015, *A&A*, **574**, A60

Thöne, C. C., Izzo, L., Flores, H., et al. 2019, arXiv:1904.05935

Tonry, J. L., Stubbs, C. W., Lykke, K. R., et al. 2012, *ApJ*, **750**, 99

Tremonti, C. A., Heckman, T. M., Kauffmann, G., et al. 2004, *ApJ*, **613**, 898

Valenti, S., Howell, D. A., Stritzinger, M. D., et al. 2016, *MNRAS*, **459**, 3939

Verheijen, M. A. W., Bershadsky, M. A., Andersen, D. R., et al. 2004, *AN*, **325**, 151

Wheeler, J. C., Johnson, V., & Clocchiatti, A. 2015, *MNRAS*, **450**, 1295

Whitesides, L., Lunnan, R., Kasliwal, M. M., et al. 2017, *ApJ*, **851**, 107

Williamson, M., Modjaz, M., & Bianco, F. B. 2019, *ApJL*, **880**, L22

Wiseman, P., Pursiainen, M., Childress, M., et al. 2020, *MNRAS*, **498**, 2575

Woosley, S., & Bloom, J. 2006, *ARA&A*, **44**, 507

Woosley, S. E. 2010, *ApJL*, **719**, L204

Zackay, B., Ofek, E. O., & Gal-Yam, A. 2016, *ApJ*, **830**, 27